MNRAS 000, 1–18 (2022) Preprint 3 August 2022 Compiled using MNRAS LATEX style file v3.0
DES-2021-0677
FERMILAB-PUB-22-558-PPD

Concerning Colour: The Effect of Environment on Type Ia Supernova Colour in the Dark Energy Survey

L. Kelsey,[1,2] M. Sullivan,[2] P. Wiseman,[2] P. Armstrong,[3] R. Chen,[4] D. Brout,[5,6] T. M. Davis,[7] M. Dixon,[8] C. Frohmaier,[1,2] L. Galbany,[9,10] O. Graur,[1] R. Kessler,[11,12] C. Lidman,[13,3] A. Möller,[8] B. Popovic,[4] B. Rose,[4] D. Scolnic,[4] M. Smith,[14] M. Vincenzi,[4] T. M. C. Abbott,[15] M. Aguena,[16] S. Allam,[17] O. Alves,[18,16] J. Annis,[17] D. Bacon,[1] E. Bertin,[19,20] S. Bocquet,[21] D. Brooks,[22] D. L. Burke,[23,24] A. Carnero Rosell,[25,16,26] M. Carrasco Kind,[27,28] J. Carretero,[29] M. Costanzi,[30,31,32] L. N. da Costa,[16] M. E. S. Pereira,[33] S. Desai,[34] H. T. Diehl,[17] S. Everett,[35] I. Ferrero,[36] J. Frieman,[17,12] J. García-Bellido,[37] D. Gruen,[21] R. A. Gruendl,[27,28] J. Gschwend,[16,38] G. Gutierrez,[17] S. R. Hinton,[7] D. L. Hollowood,[39] K. Honscheid,[40,41] D. J. James,[6] K. Kuehn,[42,43] N. Kuropatkin,[17] G. F. Lewis,[44] J. Mena-Fernández,[45] R. Miquel,[46,29] A. Palmese,[47] F. Paz-Chinchón,[27,48] A. Pieres,[16,38] A. A. Plazas Malagón,[49] M. Raveri,[50] M. Rodriguez-Monroy,[45] A. K. Romer,[51] E. Sanchez,[45] V. Scarpine,[17] M. Schubnell,[18] I. Sevilla-Noarbe,[45] E. Suchyta,[52] M. E. C. Swanson,[53] G. Tarle,[18] D. L. Tucker,[17] and N. Weaverdyck[18,54]

(DES Collaboration)

Affiliations are listed at the end of the paper

Accepted XXX. Received YYY; in original form ZZZ

ABSTRACT

Recent analyses have found intriguing correlations between the colour (c) of type Ia supernovae (SNe Ia) and the size of their mass-step, the relationship between host galaxy stellar mass and Hubble residual. These analyses suggest that the underlying cause of this relationship is dust. Using a sample of 675 photometrically-classified SNe Ia from the Dark Energy Survey 5-year sample, we study the differences in Hubble residual for a variety of host and local properties for subsamples split by their colour (c). We find a 3σ difference for the size of the mass-step when comparing blue ($c < 0$) and red ($c > 0$) SNe. We observe the lowest r.m.s. scatter (~ 0.14) in Hubble residual for blue SNe in low mass or blue environments, suggesting that these objects provide the most homogeneous sample for cosmological analyses. By fitting for c-dependent relationships between Hubble residuals and $M_{\rm stellar}$, approximating existing dust models, we remove the mass-step from the data but find significant remaining steps in rest-frame $U-R$, indicating that current dust modelling based on $M_{\rm stellar}$ may not fully explain the remaining dispersion in SN luminosity. The most dispersion is removed by instead accounting for a c-dependent relationship between Hubble residuals and global $U-R$, resulting in $\leq 1\sigma$ remaining steps in other environmental properties, suggesting that $U-R$ provides different information about the environment of SNe Ia to $M_{\rm stellar}$. This c-dependent $U-R$ relation implies that $U-R$ may be more closely linked to dust, motivating the future inclusion of galaxy $U-R$ colour in the correction for SN distance biases.

Key words: cosmology: observations – distance scale – supernovae: general – surveys

1 INTRODUCTION

The improved standardisation of type Ia supernovae (SNe Ia) is important to constrain their luminosity dispersion and gain further understanding of the dark energy equation-of-state parameter, w. By applying corrections based on empirical relationships between their brightness and light-curve width (the 'brighter-slower' relation; Rust 1974; Pskovskii 1977; Phillips 1993) and their brightness and optical colour (the 'brighter-bluer' relation; Riess et al. 1996; Tripp 1998), their luminosity dispersion can be reduced to ~ 0.14 mag (Scolnic et al. 2018). After accounting for observational uncertainties, ~ 0.08–0.10 mag of 'intrinsic dispersion' remains (e.g. Brout et al. 2019b).

In addition to these traditional light-curve corrections, there are additional correlations between the corrected SN Ia luminosity and various host galaxy 'environmental' properties. The most well-studied of these is the 'mass step' (e.g. Sullivan et al. 2010; Kelly et al. 2010; Lampeitl et al. 2010; Gupta et al. 2011; Johansson et al. 2013; Childress et al. 2013; Uddin et al. 2017, 2020; Smith et al. 2020b; Ponder et al. 2021; Popovic et al. 2021b), in which SNe Ia in more massive galaxies are more luminous after corrections than their counterparts

occurring in galaxies with lower stellar masses. This step is typically measured through differing average Hubble residuals[1] on either side of some division in environmental property, e.g. high and low stellar mass. The astrophysical reasons for this disparity are unclear, however it is known that the stellar mass ($M_{\rm stellar}$) of a galaxy correlates with the stellar ages, gas-phase and stellar metallicities, and dust content (Tremonti et al. 2004; Gallazzi et al. 2005; Garn & Best 2010; Bravo & Badenes 2011; Zahid et al. 2013), suggesting that the trends between corrected SN Ia brightness and host stellar mass could be due to differences in intrinsic SN progenitor properties (e.g., age or metallicity; Timmes et al. 2003; Röpke & Hillebrandt 2004; Kasen et al. 2009; Bravo et al. 2010) or dust (e.g., Brout & Scolnic 2021), or both. The physical nature of the dominant underlying effect remains an open question.

In addition to looking at the $M_{\rm stellar}$ of the galaxy, some studies (e.g. Lampeitl et al. 2010; Sullivan et al. 2010; D'Andrea et al. 2011; Childress et al. 2013; Pan et al. 2014; Wolf et al. 2016; Uddin et al. 2017; Kim et al. 2019; Kelsey et al. 2021) also consider other environmental properties such as the star formation rate (SFR), specific star formation rate (sSFR; SFR per unit $M_{\rm stellar}$) or rest-frame colour (e.g. $U-R$). These properties are correlated with $M_{\rm stellar}$; the most massive galaxies tend to be redder, more passive, with the lowest sSFR, whilst the lower mass galaxies tend to have more recent or ongoing star formation. These parameters provide other complementary ways to probe the stellar populations of the SN host galaxies, and may also provide insight into potential ages of the host stellar populations. Similarly sized SN luminosity steps have been found for global host galaxy sSFR, with $> 3\sigma$ evidence that SNe Ia in low sSFR galaxies are brighter on average than those in higher sSFR galaxies after corrections. The most accurate tracer to determine the relationship between magnitude and environmental property for use in cosmology remains unclear (Briday et al. 2022).

Alongside the host galaxy correlations, a wealth of studies (Rigault et al. 2013, 2015, 2020; Jones et al. 2015, 2018; Moreno-Raya et al. 2016a,b; Roman et al. 2018; Galbany et al. 2018; Rose et al. 2019; Kim et al. 2018, 2019; Kelsey et al. 2021) have shown that looking at the local region around the SN, rather than the global properties of the entire host galaxy, can provide a better understanding of the SN progenitor environment. Global galaxy properties are weighted by surface brightness, meaning that global measurements are most representative of the properties of the brightest galactic regions, and thus may not accurately descripe the true environment of the progenitor and resulting SN (Rigault et al. 2013). For example, a SN Ia may be located within a locally star forming region within a globally passive galaxy, or vice versa. Rose et al. (2021) suggest that combining corrections based on host galaxy stellar mass and local stellar age provides the best improvement to SNe Ia standardisation at $> 3\sigma$, reducing the unexplained scatter by $\sim 10\%$.

Recent analyses (Brout et al. 2019b; Smith et al. 2020b; Brout & Scolnic 2021; Kelsey et al. 2021) have shown that the magnitude of this step in average luminosity or Hubble residual with environmental property changes when considering SNe of different colours. Kelsey et al. (2021, hereafter K21) found a significant ($\sim 3\sigma$) difference between the step sizes for subsamples comprised of 'red' and 'blue' SNe Ia, with bluer SNe (defined as having a SALT2 (Guy et al. 2007, 2010) colour c of $c < 0$) being more homogeneous and displaying no significant step, whilst the redder ($c > 0$) SNe have a higher dispersion and larger step sizes.

Analyses of the underlying relationships between SN Ia colour c and the properties of their host galaxy environments have grown over the past year, with suggestion that the differing average Hubble residuals in low and high mass galaxies are caused by differences in dust properties for SNe with different c (Brout & Scolnic 2021; Popovic et al. 2021b,a). Bluer SNe ($c < 0$) will suffer less dust extinction (Jha et al. 2007) and therefore less scatter from event-to-event than red ($c > 0$) SNe. The presence of dust along the line of sight reddens the SN by differing amounts dependent on the properties of the dust, and therefore may not be the same for all SNe Ia (González-Gaitán et al. 2021; Thorp et al. 2021). There is known variation in the total-to-selective extinction ratio (R_V) along different lines of sight in the Milky Way (e.g. Schlafly et al. 2016), so logically R_V should vary between, and even within, different SNe host galaxies. This is considered in Chen et al. (2022) for a sample of DES SNe Ia in redMaGiC galaxies, and Rose et al. (2022) for a sample of Pantheon+ SNe Ia (Scolnic et al. 2021; Brout et al. 2022). Meldorf et al. (2022) suggest that a correlation between host-R_V and SNe Ia properties indicate that intrinsic scatter is driven by R_V.

An alternate explanation is that red and blue SNe Ia represent differing progenitor paths (e.g. Milne et al. 2013; Stritzinger et al. 2018; González-Gaitán et al. 2021; Kelsey et al. 2021). Blue objects are considered to be comprised of one distinct set of progenitors (hence displaying no significant step in Hubble residual across hosts of differing masses), whilst red objects are likely a combination of different progenitors or explosion mechanisms (including the blue SNe that have been reddened by dust), causing a step in Hubble residual between different mass hosts to be observed. Environmental studies may find evidence for this by analysis of the stellar population age of the region surrounding the SNe.

Regardless of the cause of the Hubble residual step, such studies indicate that blue SNe Ia, particularly those in bluer/low-mass environments, are more homogeneous and thus are better for use in cosmology (Graur et al. 2015; González-Gaitán et al. 2021; Kelsey et al. 2021).

In this study, we aim to add more weight to this argument that blue SNe Ia are more homogeneous by studying the differences in Hubble residual for subsets of SNe Ia divided by SN colour, using photometrically-confirmed SNe Ia from the Dark Energy Survey (DES) SN programme (DES-SN) five-year cosmological sample.

Our paper is structured in the following way. In Section 2, we describe the DES-SN SN Ia sample that was used in this analysis and present the method to obtain environmental properties from photometric data. We discuss the results of our study in Section 3 and Section 4, and additional analysis in Section 5. Finally, in Section 6 we summarise and conclude.

2 DATA AND METHODS

We begin by describing the SN Ia sample used in our analysis, and the methods used to obtain information about their galactic environments.

2.1 The DES-SN photometric SN Ia sample

DES is an optical imaging survey that uses four independent astrophysical probes to measure the properties of dark energy (Dark Energy Survey Collaboration et al. 2016). Here we use a sample of SNe Ia discovered by the dedicated SN programme in DES, DES-SN

[1] Hubble residual: the difference between the measured distance modulus ($\mu_{\rm obs}$) to each SN and the distance modulus calculated from the best-fit cosmology ($\mu_{\rm cosmo}$).

(Abbott et al. 2019), comprised of SNe Ia discovered in imaging data acquired by the Dark Energy Camera (DECam; Flaugher et al. 2015), mounted on the Blanco 4-m telescope at the Cerro Tololo Inter-American Observatory. The DES-SN programme was optimised for the detection of SNe Ia over the redshift range $0.2 < z < 1.2$ (Bernstein et al. 2012; Smith et al. 2020a) for use in cosmology, observing ten 3-deg^2 fields with an average cadence of 7 days in four filters ($griz$). Our sample is taken from the full five years of the survey.

This sample differs from the DES-SN three-year (DES-SN3YR) sample used in K21: it includes data from the full five years of the survey instead of only the first three years (Brout et al. 2019a), and it includes both spectroscopically-confirmed and photometrically-classified SNe Ia where the redshift for each SN is determined by a spectroscopic redshift measurement of its host galaxy. The photometry is obtained using `diffimg` (Kessler et al. 2015). DES photometric classification is outlined in Vincenzi et al. (2021) and Möller et al. (2022), with host association details in Wiseman et al. (2020).

2.1.1 SN Ia light-curve parameters

We use the SALT2 SN Ia light-curve model (Guy et al. 2007, 2010) to fit the SN Ia light curves and obtain estimates of their 'stretch' (x_1), 'colour' (c) and m_B ($-2.5\log(x_0)$, where x_0 is the fitted amplitude). SALT2 is trained with the JLA compilation SN sample, and implemented in the SNANA software package (Kessler et al. 2009). In this analysis, we use 1D BBC bias corrections (Kessler & Scolnic 2017) to correct for selection bias with a Guy et al. (2010) intrinsic scatter model (consistent with S20 and K21). We do not employ BEAMS, instead setting each P(Ia) = 1. The light curve parameters are used to calculate Hubble residuals:

$$\Delta\mu = \mu_{\rm obs} - \mu_{\rm cosmo}, \tag{1}$$

where $\mu_{\rm cosmo}$ is the fixed distance modulus calculated from a reference cosmology (flat ΛCDM with $w = -1$), and $\mu_{\rm obs}$ is the measured distance modulus (e.g., Tripp 1998; Astier et al. 2006):

$$\mu_{\rm obs} = m_B - M_0 + \alpha x_1 - \beta c + \mu_{\rm bias}, \tag{2}$$

with α, β and M_0 as nuisance parameters describing the SN population in the BBC fit.

The $\mu_{\rm bias}$ represents a correction that is applied to each SN to account for survey selection effects. This correction is typically either a '1D correction' as a function of redshift, or a '5D correction' as a function of $\{z, x_1, c, \alpha, \beta\}$ (Kessler & Scolnic 2017). The 1D correction does not account for the c-dependent selection bias (bluer SNe are brighter and easier to observe), which results in a trend of $\Delta\mu$ vs c for blue SNe. A discussion of the differences between 1D and 5D corrections with regards to host galaxy correlations in the DES-SN3YR sample can be found in Smith et al. (2020b, hereafter S20). We consider a 5D bias correction in Appendix A, finding no significant difference in our results.

In cosmological analyses, there is an additional host galaxy $M_{\rm stellar}$ correction added to Eq. 2, $\gamma G_{\rm host}$, where the nuisance parameter γ is analogous to α and β, and $G_{\rm host}$ is a step function typically located at $\log(M_{\rm stellar}/M_\odot) = 10$. We do not use this additional correction in our analysis, as we want to study the overall cause of the additional dispersion and determine if it can be explained with this simple correction.

We assume a spatially-flat ΛCDM model, with a matter density $\Omega_M = 0.3$ and Hubble constant $H_0 = 70\,{\rm km\,s^{-1}\,Mpc^{-1}}$ as a reference cosmology for the calculation of $\Delta\mu$.

2.2 SN host galaxy photometry

Here we briefly describe the DES-SN image stacking procedure and methods used to obtain photometry of each SN Ia host galaxy and region local to the SN event. The method is identical to that used in K21, and details can be found therein.

Host galaxies are assigned using the directional light radius method (DLR; Sullivan et al. 2006; Gupta et al. 2016) and are catalogued in Wiseman et al. (2020). The DLR is a measure of the separation distance between the SN and each galaxy, normalised by the apparent size of the galaxy light profile being considered (obtained from high-quality depth-optimised coadded images; Wiseman et al. 2020), in terms of the elliptical radius along a line connecting the SN to the host center.

The majority of host galaxy spectroscopic redshifts for the DES photometric sample were provided by the OzDES programme (Yuan et al. 2015; Childress et al. 2017; Lidman et al. 2020) using the Anglo-Australian Telescope (AAT). A subset of host galaxy redshifts were obtained from external catalogues of prior surveys that overlapped with the DES-SN fields. Details of host galaxy association and redshifts can be found in Vincenzi et al. (2021); Möller et al. (2022).

We use the 'seeing-optimised' DES image stacks described in K21 (created following Wiseman et al. 2020). Single-epoch exposures are added to the stack if they pass given quality cuts; for this analysis we use exposures with a τ (ratio between effective exposure time and true exposure time) of > 0.02 and a point spread function (PSF) full-width half-maximum (FWHM) $< 1.3''$ in all filters. This provides a balance between seeing and redshift coverage for our analysis.

Following K21, photometry for the host galaxy ('global' photometry) is measured using SOURCE EXTRACTOR (Bertin & Arnouts 1996) on the stacked $griz$ images.

We also measure local photometry at the SN position using a 4 kpc aperture radius following K21, based on the quality of our stacked images. Local aperture photometry is measured using APERTURE_PHOTOMETRY from the PHOTUTILS Python module (Bradley et al. 2019), and photometric uncertainties are calculated using the root-mean-square of the background-subtracted stacked images.

All our measured $griz$ fluxes are corrected for Milky Way dust extinction using colour excess $E(B-V)$ values from Schlegel et al. (1998) and multiplicative coefficients for the DES filters of $R_g = 3.186$, $R_r = 2.140$, $R_i = 1.569$ and $R_z = 1.196$ (Abbott et al. 2018), calculated using a Fitzpatrick reddening law (Fitzpatrick 1999).

2.3 SN host galaxy SED fitting

As per Smith et al. (2020b); Wiseman et al. (2020); Kelsey et al. (2021), we use spectral energy distribution (SED) fitting and templates based on the PÉGASE spectral evolution code (Fioc & Rocca-Volmerange 1997, 2019) assuming a Kroupa (2001) initial mass function (IMF) and a series of 9 smooth exponentially-declining star-formation histories, each with 102 time steps, in order to estimate the physical parameters from the photometry. Synthetic DES photometry is generated for each SED template and, using χ^2 minimisation, is matched with the measured photometry for each region (e.g., Wiseman et al. 2020). We apply a foreground dust screen with $E(B-V) = 0$ to 0.3 mag in steps of 0.05 to account for dust extinction, and only consider solutions younger than the age of the universe for each SN redshift.

From this SED fitting we obtain the stellar mass ($M_{\rm stellar}$, in $M_\odot$) and the rest-frame $UBVR$ magnitudes for all global and local regions. For each set of photometry we additionally use a Monte Carlo process

adjusting the observed photometry according to its uncertainties, with 1000 iterations in order to estimate the uncertainties in the above parameters. Full details of this process can be found in S20.

As described in K21, we apply a 'mangling' (Hsiao et al. 2007; Conley et al. 2008) correction, adjusting the best-fitting SED for each host galaxy or region using a wavelength-dependent spline multiplicative function to ensure that the SED exactly reproduces the observed photometry. This procedure allows rest-frame $UBVR$ magnitudes to be accurately calculated.

As in K21, we focus our analysis on rest-frame $U-R$. We choose this colour because it spans the greatest wavelength range in our observer-frame ($griz$) photometry (above our redshift cut, discussed in Section 2.4, we lose rest-frame R band), it is an approximate tracer of the SFR, it carries some age information of the galaxy (Trayford et al. 2016), and it correlates with galaxy morphology (correlation with $u-r$; Strateva et al. 2001; Lintott et al. 2008). By assuming that the difference in SN luminosities is due to local stellar population age, rest-frame $U-R$ has been shown to be the best photometric tracer of this parameter (Briday et al. 2022), making it highly suitable for high redshift cosmology, where spectroscopy may not be obtained of each SN environment. Furthermore, recent analyses suggest that combining environmental corrections such as global host galaxy stellar mass, and local age (potentially with colour as a proxy) may provide the best standardisation for SNe cosmology (Rose et al. 2019, 2021; Rigault et al. 2020).

2.4 SN selection requirements

From the SuperNNova classifier, we require each candidate SN Ia to have a probability of being a SN Ia of $P(Ia) > 0.5$.[2] We apply a redshift cut of $z < 0.6$, which ensures that at all redshifts the aperture size is larger than the smallest useful aperture (σ) of 0.55″ for a maximum full-width half-maximum of 1.3″ when approximating to a Gaussian. Additionally, this redshift cut minimises selection biases, particularly in the shallow fields (Kessler et al. 2019). We also apply a cut on $\sigma_{(U-R)} < 1$ mag for both the global and local measurements to have well-constrained rest-frame $U-R$ colours. This cut also removes objects with large uncertainties in $M_{\rm stellar}$ and SFR. We apply a typical 'JLA-like' (Betoule et al. 2014) light-curve selection in x_1 and c, and their associated uncertainties. A summary of the selection applied is:

- $P(Ia) > 0.5$,
- redshift $z < 0.6$,
- $(M_{\rm stellar})_{\rm global} \geq (M_{\rm stellar})_{\rm local}$,
- $\sigma_{(U-R)} < 1$ mag,
- colour $|c| < 0.3$,
- colour uncertainty $\sigma_c < 0.1$,
- stretch $|x_1| < 3$,
- stretch uncertainty $\sigma_{x_1} < 1$,
- $|\Delta\mu|/\sigma_\mu < 4$

After selection cuts, there are a total of 675 objects in our sample. From the 1484 cosmology-grade SNe Ia from Möller et al. (2022), 1152 remain after the redshift cut. The rest removed from the sample are entirely due to our quality cuts on the environmental photometry to ensure properties are well-constrained. Using a BBC fit (Section 2.1.1), we obtain values of $\alpha = 0.158 \pm 0.007$ and $\beta = 2.88 \pm 0.07$ for these data.

[2] See Appendix B for a discussion of the use of different classifiers, templates and $P(Ia)$ selection cuts.

We present the global and local photometry and derived environmental properties for the 675 SNe Ia used in this analysis in the online supplementary material. Light curves and associated environmental data for the full DES5YR sample will be released online with the cosmology data release.

3 GLOBAL AND LOCAL ENVIRONMENTS

3.1 Environmental properties and colour

We study the relationships between SN Ia colour and the SN Ia environmental properties $M_{\rm stellar}$ and rest-frame $U-R$ colour, both globally for the host galaxy, and for the 'local' 4 kpc radius regions. From Fig. 1, trends in environmental properties with c are shown, with more massive, redder galaxies and environmental regions hosting redder SNe Ia, consistent with prior (but weak) observed trends (Sullivan et al. 2010; Childress et al. 2013; Kelsey et al. 2021; Brout & Scolnic 2021; Popovic et al. 2021b). As in K21, we observe an absence of red SNe Ia in low-mass galaxies and, to a lesser extent, in bluer $U-R$ regions.

3.2 Environmental Property steps in Hubble residual

We now turn to investigating the relationships between SN Ia Hubble residuals with $M_{\rm stellar}$ and rest-frame $U-R$ colour, both globally and locally, for our DES5YR sample. We plot the Hubble residual vs. the chosen environmental property split into two bins at a chosen division point in Figure 2, and measure the mean and dispersion in Hubble residual either side of this division. The magnitude of the 'step' is simply the difference between the two means, provided with the statistical significance ($N\sigma$) of the difference. The resulting steps are presented in Table 1.

We present the step values calculated with the following step locations (division points):

- $\log(M_{\rm stellar}/M_\odot)_{\rm global} = 10.0$ (e.g., Sullivan et al. 2010)
- $\log(M_{\rm stellar}/M_\odot)_{\rm local} = 9.4$ (this value represents the median local $M_{\rm stellar}$ for this DES5YR sample)
- $(U-R)_{\rm global} = 1.0$ (K21)
- $(U-R)_{\rm local} = 1.1$ (this value represents the median local $U-R$ of this DES5YR sample, which is redder than that for K21)

K21 found that the majority (56%) of SNe in the DES3YR spectroscopically-confirmed sample were located in local regions that were bluer than their host galaxy average, with a median local $U-R = 0.95$. Using this larger sample of DES5YR photometrically-classified SNe we find a different result, 62% of SNe are located in regions that are locally redder than their host galaxy. This relationship is not redshift dependent, so is likely a feature of types of galaxies that are found to host SNe Ia in a photometric survey. DES5YR has more SNe in high mass hosts than DES3YR, and contains many more SNe with particularly low DLR measurements. For DES3YR, which was spectroscopically-confirmed, SNe spectra were required, which is difficult to obtain for SNe near the centre of their host galaxies. For DES5YR, which was photometrically-identified, spectra from the SN themselves were not needed, so more SNe in the sample are located closer to the centre of their hosts. By comparing the local $U-R$ to the DLR for DES5YR, the majority of SNe Ia that are in locally redder regions than their host galaxy average are located closer to the centre of their host galaxy. This is likely due to the colour gradients in galaxies in which elliptical and spiral galaxies are redder in the centre, getting progressively bluer outwards (e.g. Tortora et al. 2010).

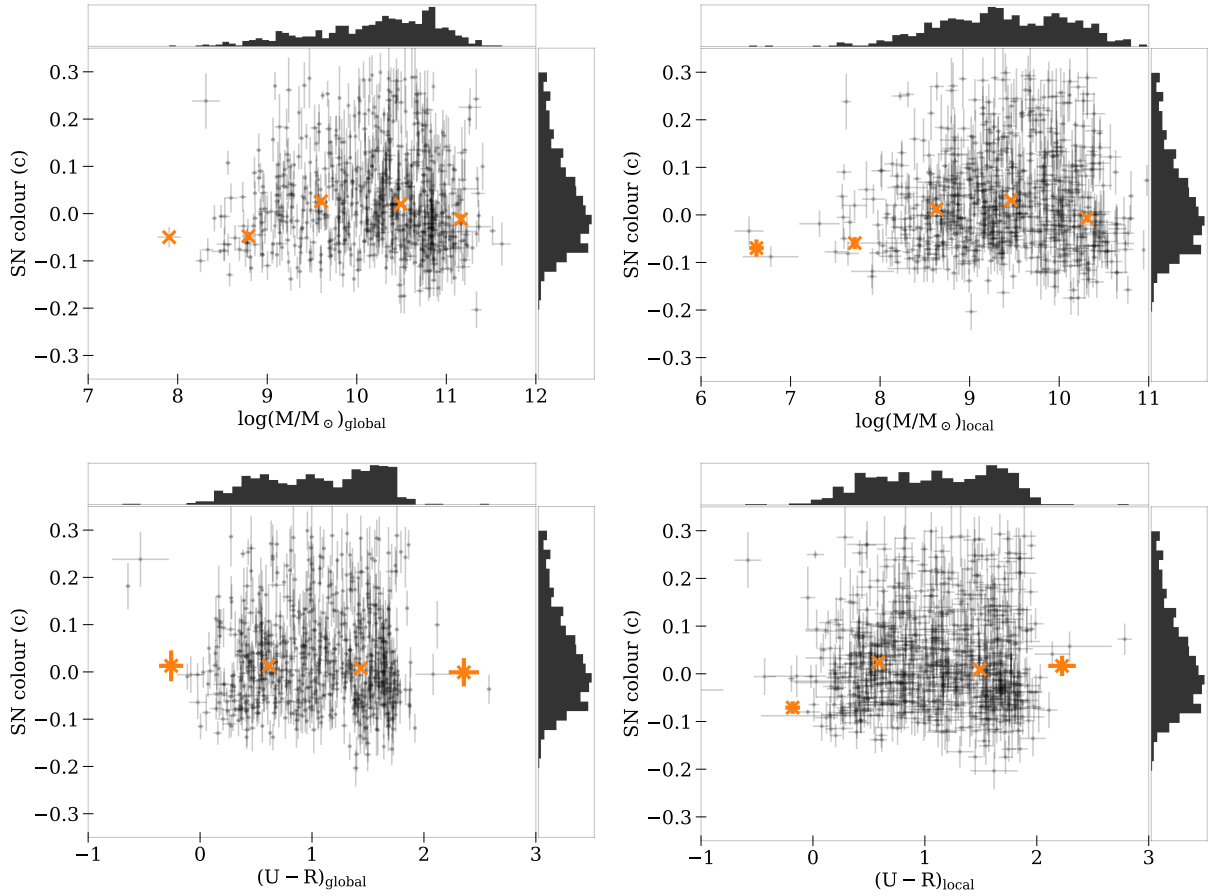

Figure 1. SN colour c as a function of both global and local environmental properties: $M_{\rm stellar}$ (upper panels) and rest-frame $U-R$ (lower panels). The orange points show the binned weighted mean colours. The histograms show the distributions of c and the environmental properties.

Table 1. Hubble residual steps, and r.m.s. scatter in Hubble residual, across both stellar mass and $U-R$ for our DES5YR sample using a 1D bias correction.

Property		Hubble Residual Step		Hubble Residual r.m.s.	
Name	Division Point	Magnitude	Sig. (σ)[b]	< DP[c]	> DP
Global Mass[a]	10.0	0.065±0.013	4.91	0.186±0.017	0.194±0.013
Local Mass	9.4	0.046±0.013	3.67	0.177±0.013	0.205±0.016
Global U-R	1.0	0.071±0.012	5.72	0.181±0.015	0.199±0.015
Local U-R	1.1	0.063±0.012	5.10	0.183±0.014	0.198±0.015

[a] Mass in $\log(M_{\rm stellar}/M_\odot)$
[b] Significance is quadrature sum.
[c] DP refers to the 'Division Point' location of the environmental property step. For example, '<DP' indicates the lower mass or bluer environments.

This is an age effect, known as the 'inside-out scenario'(e.g. Pérez et al. 2013). Star formation happens close to the galaxy centre, and over time is triggered towards the outskirts, generating an age gradient. This physical age gradient is observed in our data as a colour gradient. This colour gradient means that the average colour of a galaxy may be bluer than the colour of the central region. Without SN spectra in DES5YR, more SNe Ia in the centres of galaxies are present in the sample as shown in Figure 3, meaning that the effect of this colour gradient is more noticeable than for DES3YR. This in turn means that the median local $U-R$ is redder than for K21, and the median local $M_{\rm stellar}$ is higher, motivating our choice of division point locations for local properties.

3.2.1 $M_{\rm stellar}$

Focusing first on global $M_{\rm stellar}$, as presented in Table 1, the Hubble residual step of 0.065 ± 0.013 mag (4.9σ) agrees with prior analyses (e.g. Sullivan et al. 2010; Childress et al. 2013; Smith et al. 2020b). For local $M_{\rm stellar}$, the Hubble residual step is smaller (0.046 ± 0.013) in magnitude, but is still 3.7σ in significance. For both global and local $M_{\rm stellar}$, the r.m.s. values are lower for lower mass regions than for higher masses, consistent with K21.

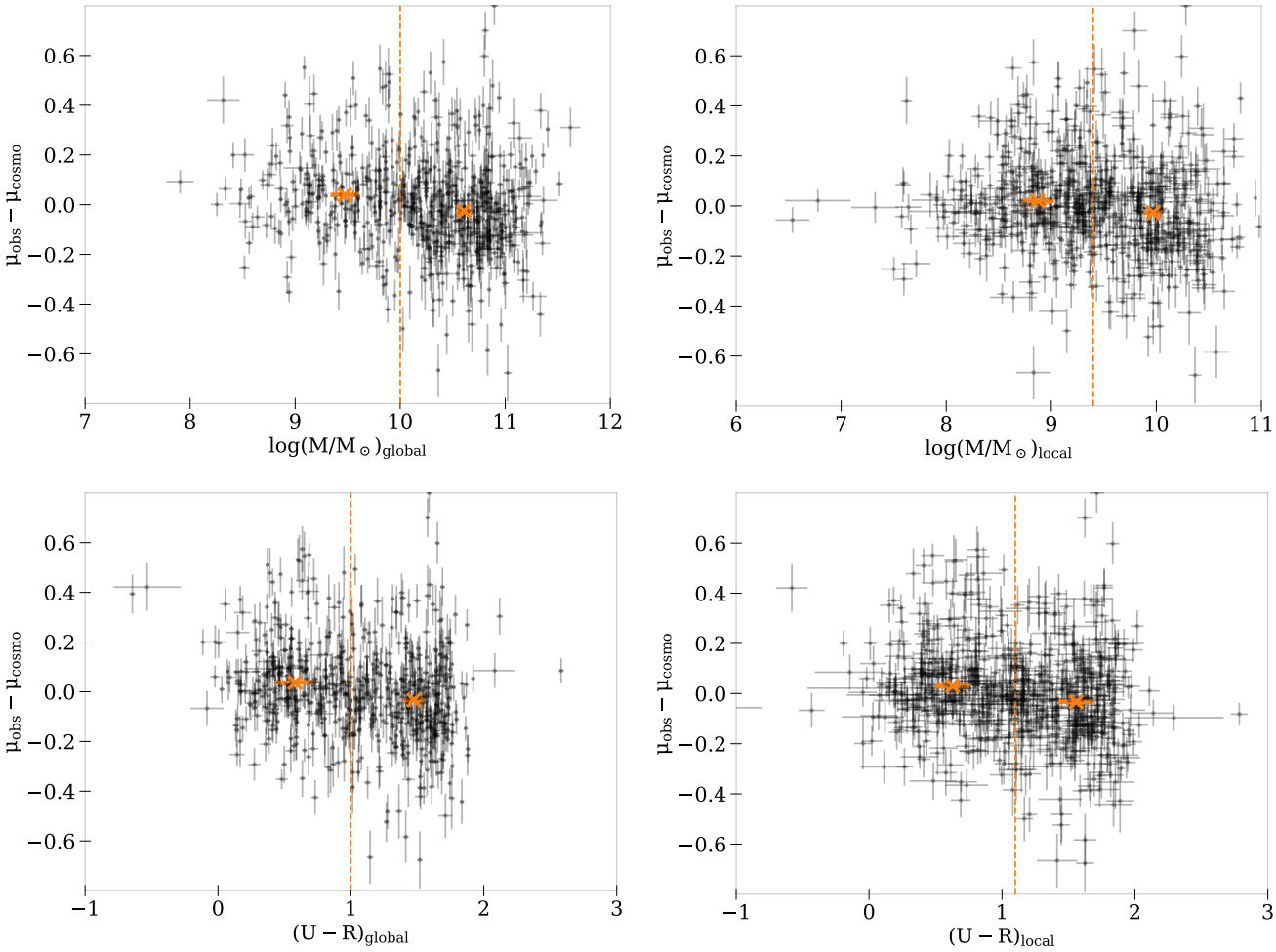

Figure 2. Hubble residual plots for DES5YR as a function of (from top to bottom and left to right): global $M_{\rm stellar}$, local $M_{\rm stellar}$ within the 4 kpc radius aperture, global rest-frame $U-R$ colour and local rest-frame $U-R$ colour. The orange dashed line is the split location, and the orange markers represent the bin means, displaying the steps in Hubble residual.

3.2.2 U − R

Moving to $U-R$, Table 1 shows that all the steps, for both local and global, are slightly smaller than, but consistent with the findings of Roman et al. (2018), Rigault et al. (2020) and K21. The global colour step (0.071 ± 0.012 mag; 5.7σ) is larger than the stellar mass steps, but the local $U-R$ (0.063 ± 0.012 mag; 5.1σ) is consistent with the global mass. Overall, the $U-R$ colour steps are fairly similar whether measured globally or locally, in agreement with K21 and Roman et al. (2018) (for $U-V$), likely due to the strong correlations between global and local colour. As in K21 and as for the stellar masses, the r.m.s. values are lower in bluer environments.

3.3 Refitting α and β

In K21, a tentative $\sim 2\sigma$ difference in optimal α and β values on each side of the environmental property division point was found. To compare with DES5YR, we refit α and β for subsamples split by $M_{\rm stellar}$ and rest-frame $U-R$. This comparison could uncover whether the steps in luminosity are driven by underlying relationships between x_1/c and environmental properties.

As can be seen in Table 2, the differences in β between subsamples with different environmental properties are the most pronounced, on the order of 3σ for all properties, with lower β values for high mass or redder regions. This difference agrees with Sullivan et al. (2011); Brout & Scolnic (2021); Kelsey et al. (2021), clearly indicating different colour-luminosity relationships for different environments. On the other hand, unlike K21, differences in α are only potentially significant for local properties, being strongest for local $M_{\rm stellar}$ ($\sim 3\sigma$). Due to the known correlation between x_1 and age (Howell et al. 2009; Neill et al. 2009; Johansson et al. 2013; Childress et al. 2014; Wiseman et al. 2021), this suggests that local properties are better age discriminators than global properties. This is likely a result of the age gradients within galaxies as discussed in Section 3.2.

4 THE EFFECT OF HOST GALAXIES ON SN COLOUR

4.1 Splitting the sample based on colour

Motivated by our findings from Section 3.3, and K21; BS21, Popovic et al. (2021b,a) which suggest that the environmental 'steps' in SN luminosity may be driven by underlying relationships between SN c and galaxy properties, we split the SN Ia sample into two based on the SN colour ($c \leq 0$ and $c > 0$), and analyse the relations between

Table 2. Differences in best-fit α and β when splitting the sample based on environmental properties.

Property	α			β		
	< DP[b]	> DP	Difference (σ)[c]	< DP	> DP	Difference (σ)
Global Mass[a]	0.16 ± 0.02	0.18 ± 0.01	0.9	3.50 ± 0.13	2.93 ± 0.09	3.6
Local Mass	0.16 ± 0.01	0.20 ± 0.01	2.8	3.38 ± 0.11	2.88 ± 0.11	3.2
Global U-R	0.17 ± 0.01	0.19 ± 0.01	1.4	3.29 ± 0.11	2.92 ± 0.10	2.5
Local U-R	0.16 ± 0.01	0.19 ± 0.01	2.1	3.43 ± 0.11	2.81 ± 0.10	3.4

[a] Mass in $\log(M_{\rm stellar}/M_\odot)$
[b] DP refers to the 'Division Point' location of the environmental property step. For example, '<DP' indicates the lower mass or bluer environments.
[c] Difference is the quadrature sum difference in α or β between subsamples.

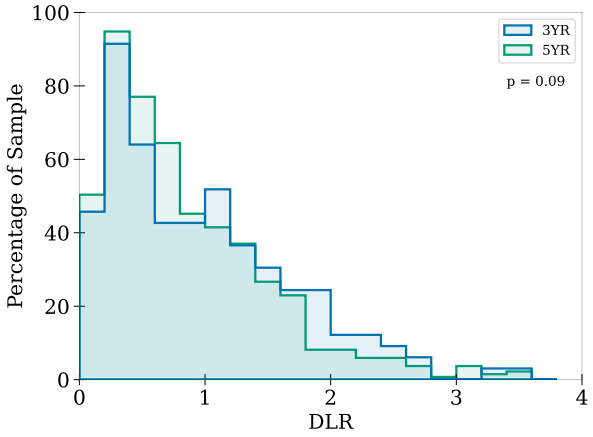

Figure 3. Distribution of DLR values for DES3YR and DES5YR, given as a percentage of individual sample sizes (DES3YR = 164, DES5YR = 675 SNe Ia), showing that a greater percentage of SNe in DES5YR are closer to the center. The mean DLR for DES3YR = 0.96, and for DES5yr = 0.86. P-value (p) = 0.09 from KS testing is displayed in the top right corner.

$\Delta\mu$ and environmental property for each subsample. We examine these relationships for both global and local host galaxy properties.

The resulting steps for local and global $M_{\rm stellar}$ and rest-frame $U-R$ for the different c subsamples are displayed in Figure 4, with numerical values given in Table 3.

In all cases, the step size is larger in red SNe Ia than in blue SNe Ia, but to varying levels of significance. There is a 3σ difference between Hubble residual step sizes for global $M_{\rm stellar}$, as also seen in K21. This difference indicates that $M_{\rm stellar}$ has a strong relationship with c, pointing to the link between host galaxy mass and dust. This is also consistent with the 3σ difference in step size for local $U-R$. The differences are not significant ($\sim 2\sigma$) for the other environmental properties, indicating a weaker link between those properties and SN c. This result is different compared to K21, where all environmental property steps have differences of $> 2\sigma$ when split into subsamples by c.

As in K21 and BS21, the r.m.s. values, presented in Table 4, for SNe Ia with $c < 0$ are considerably smaller than those for SNe Ia with $c > 0$, with the smallest values found for $c < 0$ in low stellar mass or blue environments (~ 0.14). This lends more weight to the argument posed in González-Gaitán et al. (2021) and K21 that SNe Ia in the lower mass, higher star-forming, bluer regions are a more homogeneous sample that may be better standard candles. Our sample of blue SNe Ia in blue or low $M_{\rm stellar}$ environments also have lower r.m.s. scatter than those obtained for a NIR sample (Jones et al. 2022), potentially raising questions about the necessity of space-based observations for SNe Ia cosmology.

The relationships with c and Hubble residuals are presented in a different form in Figure 5, using hexbinned heatmaps in the parameter space of environmental property and SN c, with bins shaded according to the mean Hubble residual of events in that bin. These plots show that the most homogeneous SN Ia sample with close to zero Hubble residual is in the lower left quadrants, indicating bluer SNe and low $M_{\rm stellar}$ and/or blue $U-R$ regions.

4.2 Comparison to Brout & Scolnic (2021)

BS21 suggest that the dominant component of SN Ia intrinsic scatter is caused by variation in the total-to-selective extension ratio R_V distribution as a function of host galaxy properties. They found that the Hubble residual trends with host $M_{\rm stellar}$ were modelled well by considering the SNe c distribution to be a two-component combination consisting of an intrinsic Gaussian distribution, and an extrinsic exponential $E(B-V)$ dust distribution. This extrinsic dust distribution is host galaxy $M_{\rm stellar}$ dependent, with a Gaussian R_V distribution, where mean $R_V = 2.75$ in low mass host galaxies and mean $R_V = 1.5$ in high mass hosts. The different R_V values result in different effective colour-luminosity relationships either side of the mass step division point. BS21 suggest that the mass step is therefore primarily caused by a difference in dust properties for SNe Ia with different c. This interpretation is consistent with the finding in K21 - it is physics that affects the SN colour that is driving the Hubble residual host galaxy correlations. To compare our analysis with BS21, we extend the study of SN c for different host properties, by comparing the Hubble residuals with a finer binning of SN colour, rather than simply red ($c > 0$) or blue ($c < 0$). This follows BS21 Fig. 6.

4.2.1 *Global $M_{\rm stellar}$*

First, we present the results with host galaxy $M_{\rm stellar}$ (Figure 6). Overplotted is the SN Ia sample used in BS21 (a mostly independent publicly available, spectroscopically classified, photometric light-curve sample consisting of a combination of data from the Foundation, PS1, SNLS, SDSS, CSP, CfA surveys[3], and DES3YR) with a redshift cut of $z < 0.6$ applied for consistency with our analysis. The

[3] Foundation: Foley et al. (2018), Pan-STARRS1 (PS1): Rest et al. (2014); Scolnic et al. (2018), SuperNova Legacy Survey (SNLS): Betoule et al. (2014), Sloan Digital Sky Survey (SDSS): Sako et al. (2011), Carnegie Supernova Project (CSP): Stritzinger et al. (2010), Harvard-Smithsonian Center for Astrophysics (CfA3+4): Hicken et al. (2009a,b, 2012).

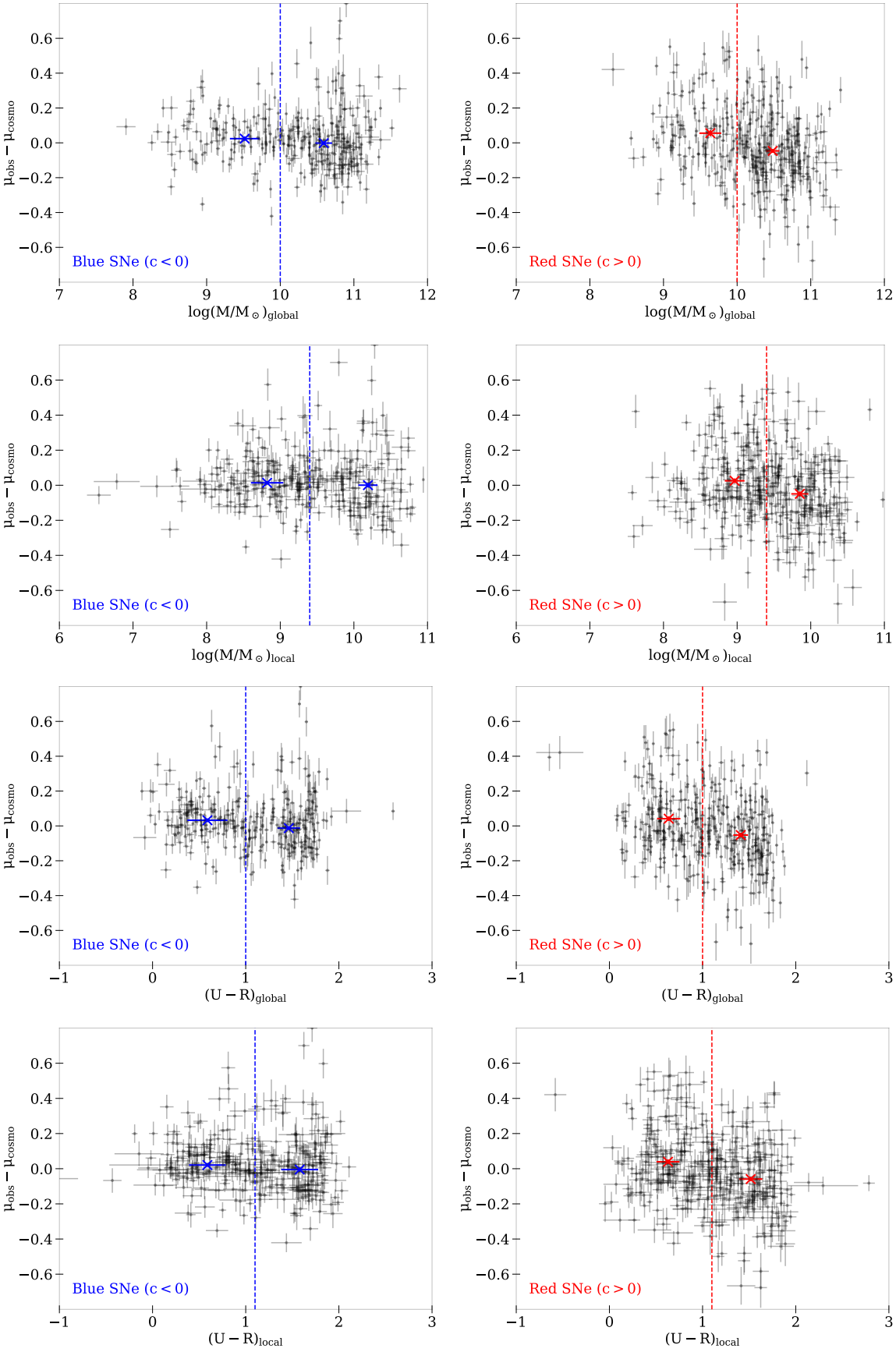

Figure 4. Hubble residuals as a function of environmental properties for subsamples split by c. The dashed lines represent the split point for each sample indicated in Table 3, defined as our location of the step, corresponding with the cross bin mean markers, displaying the steps in Hubble residual. These figures clearly show the differences in step size for red and blue SNe. Numerical values for these steps are displayed in Table 3 with r.m.s. values in Table 4.

Table 3. Subsample Hubble residual steps when splitting the sample based on c using a BBC1D correction.

Property		$c < 0$ Hubble Residual Step		$c > 0$ Hubble Residual Step		
Name	Division Point	Magnitude	Sig. (σ)[b]	Magnitude	Sig. (σ)	Difference (σ)[c]
Number of Supernovae		306		369		
Global Mass[a]	10.0	0.026 ± 0.016	1.6	0.102 ± 0.020	5.0	3.0
Local Mass	9.4	0.013 ± 0.016	0.8	0.075 ± 0.019	4.0	2.5
Global U-R	1.0	0.045 ± 0.016	2.9	0.094 ± 0.019	5.1	2.0
Local U-R	1.1	0.026 ± 0.016	1.6	0.098 ± 0.018	5.3	3.0

[a] Mass in $\log(M_{\rm stellar}/M_\odot)$
[b] Significance is quadrature sum.
[c] Difference is the quadrature sum difference in Hubble residual step magnitudes between red and blue subsamples.

Table 4. Subsample Hubble residual r.m.s scatter when splitting the sample based on c using a BBC1D correction.

Property		$c < 0$ Hubble Residual r.m.s		$c > 0$ Hubble Residual r.m.s	
Name	Division Point	$<$ DP[b]	$>$ DP	$<$ DP	$>$ DP
Global Mass[a]	10.0	0.142 ± 0.019	0.174 ± 0.017	0.216 ± 0.027	0.208 ± 0.019
Local Mass	9.4	0.142 ± 0.016	0.185 ± 0.022	0.204 ± 0.021	0.218 ± 0.023
Global U-R	1.0	0.146 ± 0.018	0.176 ± 0.019	0.205 ± 0.022	0.216 ± 0.022
Local U-R	1.1	0.141 ± 0.016	0.182 ± 0.020	0.210 ± 0.022	0.212 ± 0.022

[a] Mass in $\log(M_{\rm stellar}/M_\odot)$
[b] DP refers to the 'Division Point' location of the environmental property step. For example, '<DP' indicates the lower mass or bluer environments.

two data sets – DES5YR and BS21 – generally follow similar trends, and thus we expect that the predictions of the BS21 model will adequately model the relationships between environmental properties and c for our DES5YR sample. Figure 6(a), as in BS21 Fig. 6, shows little difference between the r.m.s. values for samples in high and low $M_{\rm stellar}$ for the bluer SNe, but this difference increases for the red SNe, also mirrored in the larger step sizes in the red bins. This increase in r.m.s. scatter and host $M_{\rm stellar}$ step size towards the redder (right hand) end of the plot suggests that the overall $M_{\rm stellar}$ step is driven by the red SNe.

We fit a variety of polynomial curves to the low and high $M_{\rm stellar}$ data points by minimising data-curve χ^2, generating simple functions for the observed $M_{\rm stellar}$ - c dependent Hubble residual relationships, so that the effect of these trends can be removed from the Hubble residuals and remaining environmental property relationships uncovered. Similarly low χ^2 values were found when fitting quadratic curves and when fitting two separate linear relations for positive and negative c, for both low and high $M_{\rm stellar}$. These linear fits resulted in similar remaining relationships once their trends were removed from the data. However, we proceed with the quadratic fits, due to the fact that they are smooth, continuous functions. There is no clear reason why the colour-luminosity relation would change dramatically at any particular c value, intuitively it is more likely to be a continuous relationship, meaning that combining linear functions for different c bins may not be as realistic. As illustrated in Figure 6(b), these quadratic fits generate simple functions for the $M_{\rm stellar}$ - c dependent Hubble residual relationships. By subtracting these curves from the Hubble residual of each SN in our sample, we correct for these observed c - dependent $M_{\rm stellar}$ trends. As shown in Table 5, this simple approximation of the BS21 dust model removes the global host galaxy mass step from our data (0.001 ± 0.013 mag; 0.1σ), however we find remaining rest-frame $U-R$ steps of 0.025 ± 0.012 mag; 2.1σ for global and 0.023 ± 0.012 mag; 1.9σ for local when the c - dependent $M_{\rm stellar}$ relation is removed, perhaps suggesting that the $M_{\rm stellar}$ dust model is not the full picture, and should include or be fully based on the $U-R$ tracer instead (see Section 4.2.2).

Whilst the remaining $U-R$ steps are small in our analysis, Roman et al. (2018) found a significant (5σ) remaining $U-V$ step when correcting first for the overall global mass step in their analysis (not dependent on c), suggesting that additional information can be provided by local properties when combined with global properties. Our results also agree with Galbany et al. (2022), where $> 2\sigma$ steps in sSFR and Hα equivalent width remain once the mass step has been corrected for, whilst a $< 2\sigma$ step in $M_{\rm stellar}$ remains once the reverse is done. This suggests that sSFH and Hα equivalent width (both related to the age of the stellar population) are better than $M_{\rm stellar}$ at improving SN Ia standardisation.

4.2.2 *Global $U-R$*

We repeated the above analysis, but starting with and fitting for the relationship between global rest-frame $U-R$ and c, instead of fitting for the global $M_{\rm stellar}$ - c dependent Hubble residual relationship. We split into 'low' and 'high' by splitting at $U-R = 1$, as motivated by K21. Again, quadratic functions fit the data best through a χ^2 minimisation, which we subtracted from the Hubble residual for each SN to correct for $U-R$ - c dependent Hubble residual relationships, as shown in panels (c) and (d) of Figure 6.

As shown in Table 5, this approximate correction removes the global $U-R$ step from the data, and we find remaining mass steps of only 0.012 ± 0.013 mag(1σ) for global $M_{\rm stellar}$ and 0.010 ± 0.012 mag(0.8σ) for local. These post-correction steps are smaller than the remaining $U-R$ steps after the global c-$M_{\rm stellar}$ relation was removed, suggesting that a $U-R$ correction encompasses more of the overall Hubble residual vs host environment relationship than the $M_{\rm stellar}$ correction; as seen in K21.

4.2.3 *Local corrections*

We repeat the corrections of Section 4.2.1 and Section 4.2.2, but for local properties instead of global, again presenting our results in Table 5.

The $\geq 3\sigma$ steps that remain in both local and global $U-R$ and in

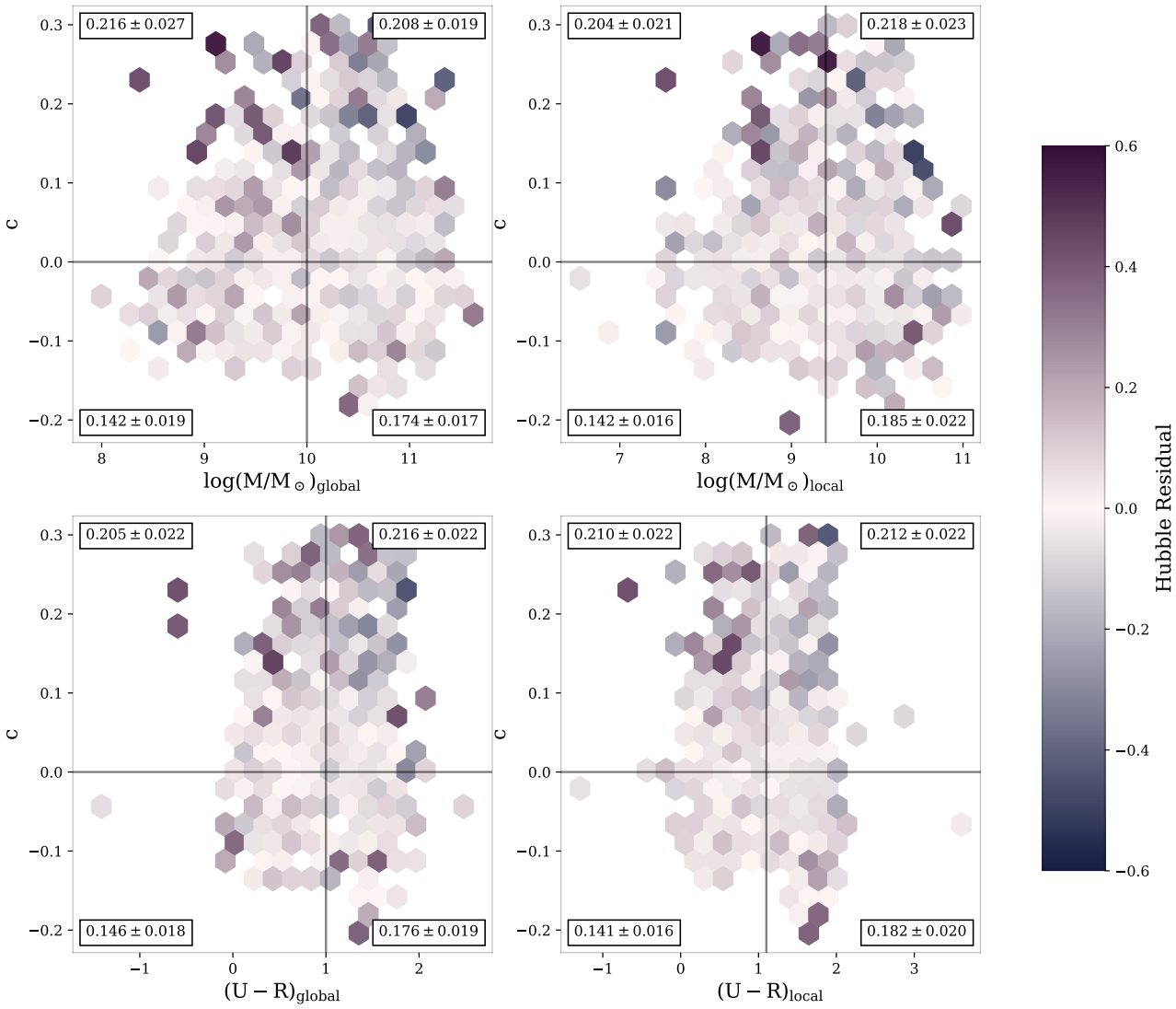

Figure 5. Hexbinned heatmaps, showing the relationships between rest-frame $U - R$ or $M_{\rm stellar}$ and c as a function of mean Hubble residual. Vertical and horizontal lines show the splits into low and high environmental property, and blue ($c \leq 0$) and red ($c > 0$) colour SNe. The numbers in each quadrant are the r.m.s. values for the SN Ia Hubble residual scatter for events in that quadrant (also in Table 4). Shown for both global (right panels) and local (left panels) $M_{\rm stellar}$ (upper panels) and rest-frame $U - R$ galaxy colour (lower panels).

Table 5. Magnitudes and significances of remaining environmental property steps when fitting for relationships between c and environmental properties using a BBC1D bias correction.

		Fitting For:			
		Host Mass	Local Mass	Host U-R	Local U-R
Remaining Step In:	Host Mass	0.001±0.013 0.1σ	0.039 ± 0.013 3.0σ	0.012 ± 0.013 1.0σ	0.023 ± 0.013 1.8σ
	Local Mass	0.011 ± 0.012 0.9σ	0.001 ± 0.012 0.1σ	0.010 ± 0.012 0.8σ	0.009 ± 0.012 0.7σ
	Host U-R	0.025 ± 0.012 2.1σ	0.047 ± 0.012 3.8σ	0.001 ± 0.012 0.1σ	0.019 ± 0.012 1.6σ
	Local U-R	0.023 ± 0.012 1.9σ	0.037 ± 0.012 3.0σ	0.006 ± 0.012 0.5σ	0.001 ± 0.012 0.1σ

All steps given in mag.
Step division points as described in Section 4.1.

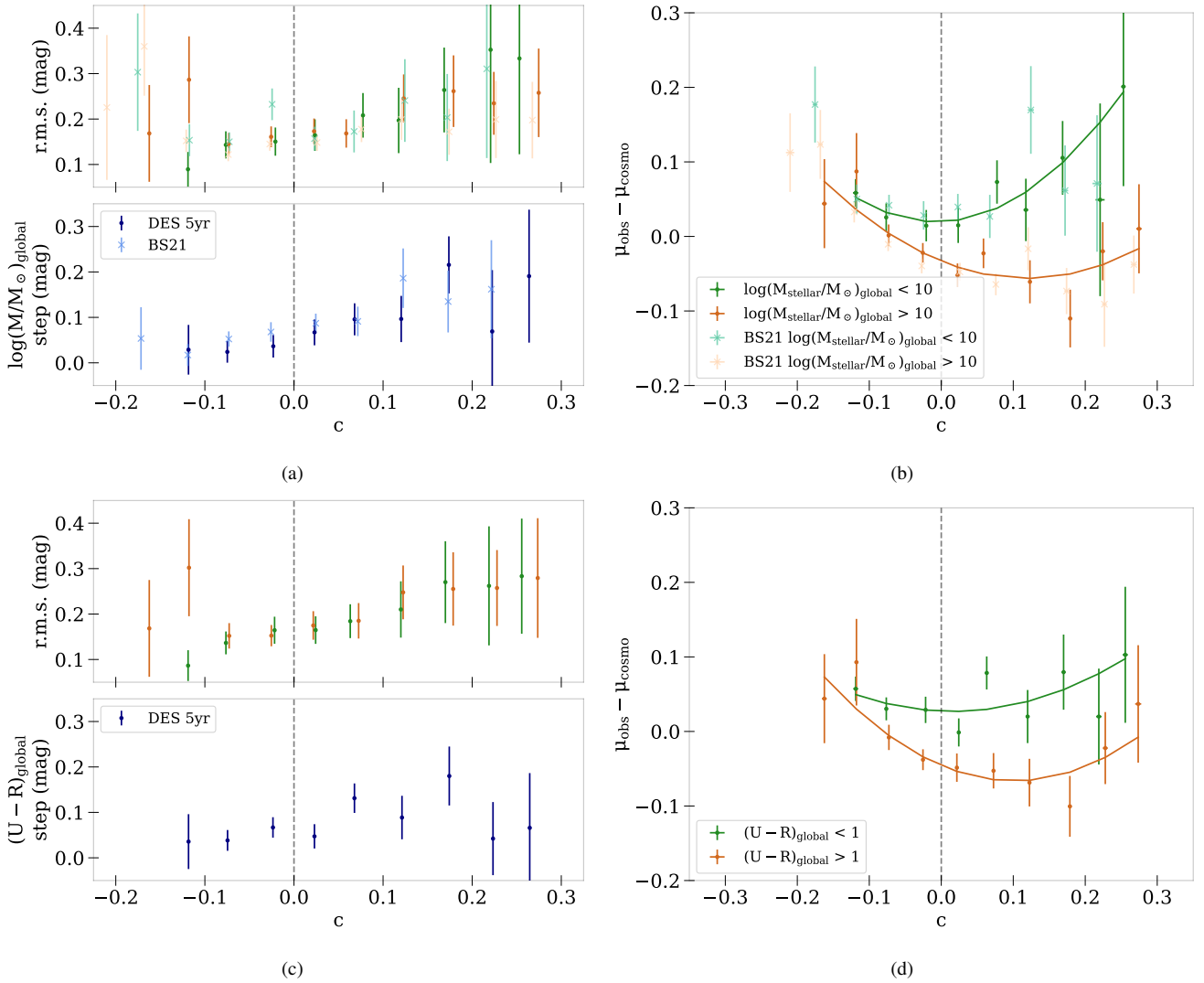

Figure 6. a) and **c)** (Upper panels) Hubble diagram r.m.s. in bins of SALT2 colour c, for SNe Ia in galaxies with high and low $M_{\rm stellar}$ a), or with high and low rest-frame $U-R$ colour c). Colour scheme corresponds with b) and d). (Lower panels) Calculated values for the size of the environmental property step as a function of c. **b)** and **d)** Binned Hubble residuals as a function of c split by host galaxy $M_{\rm stellar}$ b) and host galaxy rest-frame $U-R$ d). The overplotted quadratic fits minimise the χ^2. Data used in BS21 shown for $M_{\rm stellar}$ in a) and b) in transparent colours. BS21 do not consider $U-R$, hence is not displayed in c) and d).

global $M_{\rm stellar}$ when fitting for local $M_{\rm stellar}$ are particularly interesting. Considerable remaining steps remain once the trend with c has been removed, suggesting that local mass may not be removing any trends or perhaps is less correlated with the other parameters than expected, however this disagrees with the trends shown in K21 that local and global mass are correlated (albeit with scatter). This finding suggests that local mass may not be linked to dust in the same way as suggested by BS21 for global mass. We note in particular that local mass is the only parameter with a $< 1\sigma$ step for $c < 0$ (Table 3), so may not follow the same trends with c as the other parameters. Local mass can be understood as a stellar density, tracing the population of old stars in the region, so may be linked to age. Further investigation of this finding is needed in future study, and may require better resolved local properties than those available using DES. Higher resolution may help to determine the location of dust in the host galaxy, either contained in the local circumstellar region around a SNe, or more dispersed throughout the global host galaxy.

For local $U-R$, after fitting for the c dependent relationship, steps of $< 2\sigma$ remained in all other properties. This is likely reflective of the key result for host $U-R$, that a $U-R$ correction encompasses more of the dispersion than an $M_{\rm stellar}$ correction. Within a 4kpc radius, local $U-R$ may not be truly 'local' enough to see a clear difference compared to global $U-R$.

5 DISCUSSION

Similarly to S20, BS21 and K21, we find a $\sim 3\sigma$ significant difference between global $M_{\rm stellar}$ step sizes when splitting into subsamples based on SN c. The data agrees well with the dust explanation of BS21 and thus it is likely that the $M_{\rm stellar}$ Hubble residual step differences for c subsamples are due to the role of dust.

However, with the larger sample afforded by the DES5YR photometric sample, we see a different result to K21 with regards to global $U-R$ steps when splitting based on c. K21 found $\sim 3\sigma$ differences

in step sizes in global $U-R$ between red and blue SNe, as opposed to the smaller $\sim 2\sigma$ difference seen with this DES5YR sample.

By fitting for c-dependent global host $M_{\rm stellar}$ Hubble residual relationships in an approximation of the BS21 dust model, we are able to effectively remove the mass step from the data. Such a method has been introduced as a '4D' bias correction in Popovic et al. (2021b), and has been shown to result in a $\sigma w_{\rm sys} \sim 0.005$ (Popovic et al. 2021a). However, in this analysis we found an intriguing 2σ remaining global and local $U-R$ steps once the mass step has been removed, indicating that, whilst $M_{\rm stellar}$-based dust modelling may explain the mass step (BS21), it may not fully explain the SN luminosity dispersion. Further investigation of this tentative result is needed.

Despite $M_{\rm stellar}$ and $U-R$ being highly correlated, our analysis shows that the most Hubble residual dispersion across environmental properties was removed when correcting for a c-dependent global $U-R$ relation. As $U-R$ is connected to stellar age, this is expected given an older stellar population is one in which a larger fraction of the hotter stars have had time to explode and create dust. This result motivates further work into integrating mass and age simultaneously into scatter models and bias correction, with initial investigations presented in Wiseman et al. (2022).

5.1 Impact on Cosmology

Based on this analysis, our suggestion for future cosmology analyses is to correct for a global c-dependent $U-R$ effect as this removes the most dispersion in all other environmental properties. Alternatively, corrections could be combined to remove more dispersion than one correction alone. To reduce potential bias in the standardisation, these should be simultaneously fit with the other light-curve standardisation parameters (Rose et al. 2021; Dixon 2021).

However, given the homogeneity of blue ($c < 0$) supernovae in low mass or locally blue environments (as shown in Table 4 and Figure 5), it may be simplest and of most immediate value to use these SNe in cosmology (Kelsey et al. 2021; González-Gaitán et al. 2021), mitigating the need for environment correction. This is not a new suggestion, and there is a wealth of information pointing to the benefits of such a cut. For example, Rigault et al. (2013) postulate that SNe Ia from locally passive environments are the cause of the biases they observed due to their higher scatter, and they suggest adding a selection cut to only include those in locally star forming (i.e. blue) environments for cosmology. This is emphasised by Childress et al. (2014), Kelly et al. (2015), Henne et al. (2017) and Kim et al. (2018) who all find consistent results, and make the same conclusions about selecting star forming galaxies. Graur et al. (2015) and Kim et al. (2018) both suggest that the scatter is further constrained by limiting to low-mass ($\leq 10^{10} M_{\odot}$) globally star-forming host galaxies. In another test, through the analysis of ejecta velocities, Wang et al. (2009), Foley & Kasen (2011) and Siebert et al. (2020) all find that the SN scatter can be reduced by using lower-velocity, bluer supernovae. By combining all of this knowledge from previous analyses, and the confirmations from K21, González-Gaitán et al. (2021) and this study, we should use a subset of blue ($c < 0$) SNe in low mass/blue/star-forming environments to provide the most homogeneous sample for future cosmology.

6 SUMMARY

By expanding the findings of our previous study into the relationship between SNIa host environment and c (K21) to a larger sample consisting of SNIa from DES5YR, we have provided more weight to suggestions for future cosmological analyses, and have added our point of view to the historic mass vs age debate.

From our analysis our key findings are as follows:

(i) Hubble residual steps in environmental properties are consistent with prior analyses, with values of $\sim 5\sigma$ for global $M_{\rm stellar}$, and for global and local rest-frame $U-R$. The local mass step is slightly smaller at $\sim 4\sigma$.

(ii) When splitting our data into subsamples based on c, the largest, and most statistically significant, differences in Hubble residual 'step' are associated with host $M_{\rm stellar}$ and local $U-R$, agreeing with K21.

(iii) As in K21 and González-Gaitán et al. (2021), we observe the lowest rms scatter, and thus highest homogeneity for blue ($c < 0$) supernovae in low mass or blue environments. This suggests that such a subsample of supernovae may provide the best sample for use in future cosmological analyses.

(iv) Despite removing the mass step, intriguing 2σ steps in global and local $U-R$ remain after fitting for a simple approximation of the BS21 dust model. This suggests that current dust modelling may not fully explain the dispersion in SN luminosity.

(v) The dispersion is minimised considering a c-dependent global $U-R$ relation, implying that $U-R$ provides different information about the environment of SNe Ia than $M_{\rm stellar}$, and thus may be more linked to dust.

This analysis has important cosmological implications, which should be taken into account in the next generation of cosmological analyses. On one hand, the homogeneity of blue SNe in low mass or blue environments provides more weight to the argument that they are the best subsample to use for precision cosmology, so it may simply be easiest to just use those. On the other hand, to gain insight into the true astrophysical cause of the SNe Ia dispersion, combining environmental corrections or studying the impact of dust on galaxy $U-R$ may provide the answers for the true relationships between SNe Ia and their environments.

ACKNOWLEDGEMENTS

This work was supported by the Science and Technology Facilities Council [grant number ST/P006760/1] through the DISCnet Centre for Doctoral Training. L.K. thanks the UKRI Future Leaders Fellowship for support through the grant MR/T01881X/1. M.S. acknowledges from EU/FP7-ERC grant 615929, and P.W. acknowledges support from STFC grant ST/R000506/1. L.G. acknowledges financial support from the Spanish Ministerio de Ciencia e Innovación (MCIN), the Agencia Estatal de Investigación (AEI) 10.13039/501100011033, and the European Social Fund (ESF) "Investing in your future" under the 2019 Ramón y Cajal program RYC2019-027683-I and the PID2020-115253GA-I00 HOSTFLOWS project, from Centro Superior de Investigaciones Científicas (CSIC) under the PIE project 20215AT016, and the program Unidad de Excelencia María de Maeztu CEX2020-001058-M.

This research made use of Astropy,[4] a community-developed core Python package for Astronomy (Astropy Collaboration et al. 2013; Price-Whelan et al. 2018). This research made use of Photutils, an Astropy package for detection and photometry of astronomical sources (Bradley et al. 2019).

[4] http://www.astropy.org

Funding for the DES Projects has been provided by the U.S. Department of Energy, the U.S. National Science Foundation, the Ministry of Science and Education of Spain, the Science and Technology Facilities Council of the United Kingdom, the Higher Education Funding Council for England, the National Center for Supercomputing Applications at the University of Illinois at Urbana-Champaign, the Kavli Institute of Cosmological Physics at the University of Chicago, the Center for Cosmology and Astro-Particle Physics at the Ohio State University, the Mitchell Institute for Fundamental Physics and Astronomy at Texas A&M University, Financiadora de Estudos e Projetos, Fundação Carlos Chagas Filho de Amparo à Pesquisa do Estado do Rio de Janeiro, Conselho Nacional de Desenvolvimento Científico e Tecnológico and the Ministério da Ciência, Tecnologia e Inovação, the Deutsche Forschungsgemeinschaft and the Collaborating Institutions in the Dark Energy Survey.

The Collaborating Institutions are Argonne National Laboratory, the University of California at Santa Cruz, the University of Cambridge, Centro de Investigaciones Energéticas, Medioambientales y Tecnológicas-Madrid, the University of Chicago, University College London, the DES-Brazil Consortium, the University of Edinburgh, the Eidgenössische Technische Hochschule (ETH) Zürich, Fermi National Accelerator Laboratory, the University of Illinois at Urbana-Champaign, the Institut de Ciències de l'Espai (IEEC/CSIC), the Institut de Física d'Altes Energies, Lawrence Berkeley National Laboratory, the Ludwig-Maximilians Universität München and the associated Excellence Cluster Universe, the University of Michigan, the National Optical Astronomy Observatory, the University of Nottingham, The Ohio State University, the University of Pennsylvania, the University of Portsmouth, SLAC National Accelerator Laboratory, Stanford University, the University of Sussex, Texas A&M University, and the OzDES Membership Consortium.

Based in part on observations at Cerro Tololo Inter-American Observatory, National Optical Astronomy Observatory, which is operated by the Association of Universities for Research in Astronomy (AURA) under a cooperative agreement with the National Science Foundation.

The DES data management system is supported by the National Science Foundation under Grant Numbers AST-1138766 and AST-1536171. The DES participants from Spanish institutions are partially supported by MINECO under grants AYA2015-71825, ESP2015-66861, FPA2015-68048, SEV-2016-0588, SEV-2016-0597, and MDM-2015-0509, some of which include ERDF funds from the European Union. IFAE is partially funded by the CERCA program of the Generalitat de Catalunya. Research leading to these results has received funding from the European Research Council under the European Union's Seventh Framework Program (FP7/2007-2013) including ERC grant agreements 240672, 291329, and 306478. We acknowledge support from the Brazilian Instituto Nacional de Ciência e Tecnologia (INCT) e-Universe (CNPq grant 465376/2014-2).

This manuscript has been authored by Fermi Research Alliance, LLC under Contract No. DE-AC02-07CH11359 with the U.S. Department of Energy, Office of Science, Office of High Energy Physics.

DATA AVAILABILITY

The global and local photometry and derived environmental properties for the 675 SNe presented in this analysis are available in the online supplementary material. The light curves for the full DES-SN photometric SN Ia catalogue and associated host galaxy data will be made available as part of the DES5YR SN cosmology analysis at https://des.ncsa.illinois.edu/releases/sn.

REFERENCES

Abbott T. M. C., et al., 2018, ApJS, 239, 18
Abbott T. M. C., et al., 2019, ApJ, 872, L30
Astier P., et al., 2006, A&A, 447, 31
Astropy Collaboration et al., 2013, A&A, 558, A33
Bernstein J. P., et al., 2012, ApJ, 753, 152
Bertin E., Arnouts S., 1996, A&AS, 117, 393
Betoule M., et al., 2014, A&A, 568, A22
Bradley L., et al., 2019, astropy/photutils: v0.6, doi:10.5281/zenodo.2533376, https://doi.org/10.5281/zenodo.2533376
Bravo E., Badenes C., 2011, MNRAS, 414, 1592
Bravo E., Domínguez I., Badenes C., Piersanti L., Straniero O., 2010, ApJ, 711, L66
Briday M., et al., 2022, A&A, 657, A22
Brout D., Scolnic D., 2021, ApJ, 909, 26
Brout D., et al., 2019a, ApJ, 874, 106
Brout D., et al., 2019b, ApJ, 874, 150
Brout D., et al., 2022, arXiv e-prints, p. arXiv:2202.04077
Chen R., et al., 2022, arXiv e-prints, p. arXiv:2202.10480
Childress M., et al., 2013, ApJ, 770, 108
Childress M. J., Wolf C., Zahid H. J., 2014, MNRAS, 445, 1898
Childress M. J., et al., 2017, MNRAS, 472, 273
Conley A., et al., 2008, ApJ, 681, 482
D'Andrea C. B., et al., 2011, ApJ, 743, 172
Dai M., Kuhlmann S., Wang Y., Kovacs E., 2018, MNRAS, 477, 4142
Dark Energy Survey Collaboration et al., 2016, MNRAS, 460, 1270
Dixon S., 2021, PASP, 133, 054501
Fioc M., Rocca-Volmerange B., 1997, A&A, 500, 507
Fioc M., Rocca-Volmerange B., 2019, A&A, 623, A143
Fitzpatrick E. L., 1999, PASP, 111, 63
Flaugher B., et al., 2015, AJ, 150, 150
Foley R. J., Kasen D., 2011, ApJ, 729, 55
Foley R. J., et al., 2018, MNRAS, 475, 193
Galbany L., et al., 2018, ApJ, 855, 107
Galbany L., et al., 2022, A&A, 659, A89
Gallazzi A., Charlot S., Brinchmann J., White S. D. M., Tremonti C. A., 2005, MNRAS, 362, 41
Garn T., Best P. N., 2010, MNRAS, 409, 421
González-Gaitán S., de Jaeger T., Galbany L., Mourão A., Paulino-Afonso A., Filippenko A. V., 2021, MNRAS, 508, 4656
Graur O., Bianco F. B., Modjaz M., 2015, MNRAS, 450, 905
Gupta R. R., et al., 2011, ApJ, 740, 92
Gupta R. R., et al., 2016, AJ, 152, 154
Guy J., et al., 2007, A&A, 466, 11
Guy J., et al., 2010, A&A, 523, A7
Henne V., et al., 2017, New Astronomy, 51, 43
Hicken M., et al., 2009a, ApJ, 700, 331
Hicken M., Wood-Vasey W. M., Blondin S., Challis P., Jha S., Kelly P. L., Rest A., Kirshner R. P., 2009b, ApJ, 700, 1097
Hicken M., et al., 2012, ApJS, 200, 12
Hounsell R., Sako M., 2022, in prep
Howell D. A., et al., 2009, ApJ, 691, 661
Hsiao E. Y., Conley A., Howell D. A., Sullivan M., Pritchet C. J., Carlberg R. G., Nugent P. E., Phillips M. M., 2007, ApJ, 663, 1187
Jha S., Riess A. G., Kirshner R. P., 2007, ApJ, 659, 122
Johansson J., et al., 2013, MNRAS, 435, 1680
Jones D. O., Riess A. G., Scolnic D. M., 2015, ApJ, 812, 31
Jones D. O., et al., 2017, ApJ, 843, 6
Jones D. O., et al., 2018, ApJ, 867, 108
Jones D. O., et al., 2022, ApJ, 933, 172
Kasen D., Röpke F. K., Woosley S. E., 2009, Nature, 460, 869
Kelly P. L., Hicken M., Burke D. L., Mandel K. S., Kirshner R. P., 2010, ApJ, 715, 743

Kelly P. L., Filippenko A. V., Burke D. L., Hicken M., Ganeshalingam M., Zheng W., 2015, Science, 347, 1459
Kelsey L., et al., 2021, MNRAS, 501, 4861
Kessler R., Scolnic D., 2017, ApJ, 836, 56
Kessler R., et al., 2009, PASP, 121, 1028
Kessler R., et al., 2015, AJ, 150, 172
Kessler R., et al., 2019, MNRAS, 485, 1171
Kim Y.-L., Smith M., Sullivan M., Lee Y.-W., 2018, ApJ, 854, 24
Kim Y.-L., Kang Y., Lee Y.-W., 2019, Journal of Korean Astronomical Society, 52, 181
Kroupa P., 2001, MNRAS, 322, 231
Lampeitl H., et al., 2010, ApJ, 722, 566
Lidman C., et al., 2020, MNRAS, 496, 19
Lintott C. J., et al., 2008, MNRAS, 389, 1179
Meldorf C., et al., 2022, arXiv e-prints, p. arXiv:2206.06928
Milne P. A., Brown P. J., Roming P. W. A., Bufano F., Gehrels N., 2013, ApJ, 779, 23
Möller A., de Boissière T., 2020, MNRAS, 491, 4277
Möller A., et al., 2022, MNRAS, 514, 5159
Moreno-Raya M. E., López-Sánchez Á. R., Mollá M., Galbany L., Vílchez J. M., Carnero A., 2016a, MNRAS, 462, 1281
Moreno-Raya M. E., Mollá M., López-Sánchez Á. R., Galbany L., Vílchez J. M., Carnero Rosell A., Domínguez I., 2016b, ApJ, 818, L19
Neill J. D., et al., 2009, ApJ, 707, 1449
Pan Y. C., et al., 2014, MNRAS, 438, 1391
Pérez E., et al., 2013, ApJ, 764, L1
Phillips M. M., 1993, ApJ, 413, L105
Ponder K. A., Wood-Vasey W. M., Weyant A., Barton N. T., Galbany L., Liu S., Garnavich P., Matheson T., 2021, ApJ, 923, 197
Popovic B., Brout D., Kessler R., Scolnic D., 2021a, arXiv e-prints, p. arXiv:2112.04456
Popovic B., Brout D., Kessler R., Scolnic D., Lu L., 2021b, ApJ, 913, 49
Price-Whelan A. M., et al., 2018, AJ, 156, 123
Pskovskii I. P., 1977, Soviet Ast., 21, 675
Rest A., et al., 2014, ApJ, 795, 44
Riess A. G., Press W. H., Kirshner R. P., 1996, ApJ, 473, 88
Rigault M., et al., 2013, A&A, 560, A66
Rigault M., et al., 2015, ApJ, 802, 20
Rigault M., et al., 2020, A&A, 644, A176
Roman M., et al., 2018, A&A, 615, A68
Röpke F. K., Hillebrandt W., 2004, A&A, 420, L1
Rose B. M., Garnavich P. M., Berg M. A., 2019, ApJ, 874, 32
Rose B. M., Rubin D., Strolger L., Garnavich P. M., 2021, ApJ, 909, 28
Rose B. M., Popovic B., Scolnic D., Brout D., 2022, arXiv e-prints, p. arXiv:2206.09950
Rust B. W., 1974, PhD thesis, Oak Ridge National Laboratory, Tennessee
Sako M., et al., 2011, ApJ, 738, 162
Schlafly E. F., et al., 2016, ApJ, 821, 78
Schlegel D. J., Finkbeiner D. P., Davis M., 1998, ApJ, 500, 525
Scolnic D. M., et al., 2018, ApJ, 859, 101
Scolnic D., et al., 2021, arXiv e-prints, p. arXiv:2112.03863
Siebert M. R., Foley R. J., Jones D. O., Davis K. W., 2020, MNRAS, 493, 5713
Smith M., et al., 2020a, AJ, 160, 267
Smith M., et al., 2020b, MNRAS, 494, 4426
Strateva I., et al., 2001, AJ, 122, 1861
Stritzinger M., et al., 2010, AJ, 140, 2036
Stritzinger M. D., et al., 2018, ApJ, 864, L35
Sullivan M., et al., 2006, ApJ, 648, 868
Sullivan M., et al., 2010, MNRAS, 406, 782
Sullivan M., et al., 2011, ApJ, 737, 102
Thorp S., Mandel K. S., Jones D. O., Ward S. M., Narayan G., 2021, MNRAS, 508, 4310
Timmes F. X., Brown E. F., Truran J. W., 2003, ApJ, 590, L83
Tortora C., Napolitano N. R., Cardone V. F., Capaccioli M., Jetzer P., Molinaro R., 2010, MNRAS, 407, 144
Trayford J. W., Theuns T., Bower R. G., Crain R. A., Lagos C. d. P., Schaller M., Schaye J., 2016, MNRAS, 460, 3925
Tremonti C. A., et al., 2004, ApJ, 613, 898
Tripp R., 1998, A&A, 331, 815
Uddin S. A., Mould J., Lidman C., Ruhlmann-Kleider V., Zhang B. R., 2017, ApJ, 848, 56
Uddin S. A., et al., 2020, ApJ, 901, 143
Vincenzi M., Sullivan M., Firth R. E., Gutiérrez C. P., Frohmaier C., Smith M., Angus C., Nichol R. C., 2019, MNRAS, 489, 5802
Vincenzi M., et al., 2021, MNRAS, 505, 2819
Wang X., et al., 2009, ApJ, 699, L139
Wiseman P., et al., 2020, MNRAS, 495, 4040
Wiseman P., et al., 2021, MNRAS, 506, 3330
Wiseman P., et al., 2022, arXiv e-prints, p. arXiv:2207.05583
Wolf R. C., et al., 2016, ApJ, 821, 115
Yuan F., et al., 2015, MNRAS, 452, 3047
Zahid H. J., Yates R. M., Kewley L. J., Kudritzki R. P., 2013, ApJ, 763, 92

[1] Institute of Cosmology and Gravitation, University of Portsmouth, Portsmouth, PO1 3FX, UK
[2] School of Physics and Astronomy, University of Southampton, Southampton, SO17 1BJ, UK
[3] The Research School of Astronomy and Astrophysics, Australian National University, ACT 2601, Australia
[4] Department of Physics, Duke University Durham, NC 27708, USA
[5] Einstein Fellow
[6] Center for Astrophysics | Harvard & Smithsonian, 60 Garden Street, Cambridge, MA 02138, USA
[7] School of Mathematics and Physics, University of Queensland, Brisbane, QLD 4072, Australia
[8] Centre for Astrophysics & Supercomputing, Swinburne University of Technology, Victoria 3122, Australia
[9] Institut d'Estudis Espacials de Catalunya (IEEC), 08034 Barcelona, Spain
[10] Institute of Space Sciences (ICE, CSIC), Campus UAB, Carrer de Can Magrans, s/n, 08193 Barcelona, Spain
[11] Department of Astronomy and Astrophysics, University of Chicago, Chicago, IL 60637, USA
[12] Kavli Institute for Cosmological Physics, University of Chicago, Chicago, IL 60637, USA
[13] Centre for Gravitational Astrophysics, College of Science, The Australian National University, ACT 2601, Australia
[14] Univ Lyon, Univ Claude Bernard Lyon 1, CNRS, IP2I Lyon / IN2P3, IMR 5822, F-69622 Villeurbanne, France
[15] Cerro Tololo Inter-American Observatory, NSF's National Optical-Infrared Astronomy Research Laboratory, Casilla 603, La Serena, Chile
[16] Laboratório Interinstitucional de e-Astronomia - LIneA, Rua Gal. José Cristino 77, Rio de Janeiro, RJ - 20921-400, Brazil
[17] Fermi National Accelerator Laboratory, P. O. Box 500, Batavia, IL 60510, USA
[18] Department of Physics, University of Michigan, Ann Arbor, MI 48109, USA
[19] CNRS, UMR 7095, Institut d'Astrophysique de Paris, F-75014, Paris, France
[20] Sorbonne Universités, UPMC Univ Paris 06, UMR 7095, Institut d'Astrophysique de Paris, F-75014, Paris, France
[21] University Observatory, Faculty of Physics, Ludwig-Maximilians-Universität, Scheinerstr. 1, 81679 Munich, Germany
[22] Department of Physics & Astronomy, University College London, Gower Street, London, WC1E 6BT, UK

[23] Kavli Institute for Particle Astrophysics & Cosmology, P. O. Box 2450, Stanford University, Stanford, CA 94305, USA
[24] SLAC National Accelerator Laboratory, Menlo Park, CA 94025, USA
[25] Instituto de Astrofisica de Canarias, E-38205 La Laguna, Tenerife, Spain
[26] Universidad de La Laguna, Dpto. Astrofísica, E-38206 La Laguna, Tenerife, Spain
[27] Center for Astrophysical Surveys, National Center for Supercomputing Applications, 1205 West Clark St., Urbana, IL 61801, USA
[28] Department of Astronomy, University of Illinois at Urbana-Champaign, 1002 W. Green Street, Urbana, IL 61801, USA
[29] Institut de Física d'Altes Energies (IFAE), The Barcelona Institute of Science and Technology, Campus UAB, 08193 Bellaterra (Barcelona) Spain
[30] Astronomy Unit, Department of Physics, University of Trieste, via Tiepolo 11, I-34131 Trieste, Italy
[31] INAF-Osservatorio Astronomico di Trieste, via G. B. Tiepolo 11, I-34143 Trieste, Italy
[32] Institute for Fundamental Physics of the Universe, Via Beirut 2, 34014 Trieste, Italy
[33] Hamburger Sternwarte, Universität Hamburg, Gojenbergsweg 112, 21029 Hamburg, Germany
[34] Department of Physics, IIT Hyderabad, Kandi, Telangana 502285, India
[35] Jet Propulsion Laboratory, California Institute of Technology, 4800 Oak Grove Dr., Pasadena, CA 91109, USA
[36] Institute of Theoretical Astrophysics, University of Oslo. P.O. Box 1029 Blindern, NO-0315 Oslo, Norway
[37] Instituto de Fisica Teorica UAM/CSIC, Universidad Autonoma de Madrid, 28049 Madrid, Spain
[38] Observatório Nacional, Rua Gal. José Cristino 77, Rio de Janeiro, RJ - 20921-400, Brazil
[39] Santa Cruz Institute for Particle Physics, Santa Cruz, CA 95064, USA
[40] Center for Cosmology and Astro-Particle Physics, The Ohio State University, Columbus, OH 43210, USA
[41] Department of Physics, The Ohio State University, Columbus, OH 43210, USA
[42] Australian Astronomical Optics, Macquarie University, North Ryde, NSW 2113, Australia
[43] Lowell Observatory, 1400 Mars Hill Rd, Flagstaff, AZ 86001, USA
[44] Sydney Institute for Astronomy, School of Physics, A28, The University of Sydney, NSW 2006, Australia
[45] Centro de Investigaciones Energéticas, Medioambientales y Tecnológicas (CIEMAT), Madrid, Spain
[46] Institució Catalana de Recerca i Estudis Avançats, E-08010 Barcelona, Spain
[47] Department of Astronomy, University of California, Berkeley, 501 Campbell Hall, Berkeley, CA 94720, USA
[48] Institute of Astronomy, University of Cambridge, Madingley Road, Cambridge CB3 0HA, UK
[49] Department of Astrophysical Sciences, Princeton University, Peyton Hall, Princeton, NJ 08544, USA
[50] Department of Physics and Astronomy, University of Pennsylvania, Philadelphia, PA 19104, USA
[51] Department of Physics and Astronomy, Pevensey Building, University of Sussex, Brighton, BN1 9QH, UK
[52] Computer Science and Mathematics Division, Oak Ridge National Laboratory, Oak Ridge, TN 37831
[53] National Center for Supercomputing Applications, 1205 West Clark St., Urbana, IL 61801, USA
[54] Lawrence Berkeley National Laboratory, 1 Cyclotron Road, Berkeley, CA 94720, USA

Table A1. Hubble residual steps for stellar mass and $U-R$ for the DES5YR data using a 5D bias correction.

Property		Hubble Residual Step		Hubble Residual r.m.s.	
Name	Division Point	Magnitude	Sig. (σ)[b]	< DP[c]	> DP
Global Mass[a]	10.0	0.057±0.012	4.67	0.174±0.016	0.171±0.012
Local Mass	9.4	0.037±0.012	3.17	0.161±0.012	0.183±0.014
Global U-R	1.0	0.061±0.011	5.40	0.170±0.014	0.173±0.013
Local U-R	1.1	0.053±0.011	4.70	0.170±0.013	0.173±0.013

[a] Mass in $\log(M_{\rm stellar}/M_{\odot})$
[b] Significance is quadrature sum.
[c] DP refers to the 'Division Point' location of the environmental property step. For example, '<DP' indicates the lower mass or bluer environments.

Table A2. Subsample data when splitting the sample based on c using a 5D bias correction.

Property		$c<0$ Hubble Residual Step		$c>0$ Hubble Residual Step		
Name	Division Point	Magnitude	Sig. (σ)[b]	Magnitude	Sig. (σ)	Difference (σ)[c]
Number of Supernovae		306		366		
Global Mass[a]	10.0	0.026 ± 0.016	1.7	0.088 ± 0.018	4.8	2.6
Local Mass	9.4	0.010 ± 0.015	0.7	0.061 ± 0.017	3.6	2.2
Global U-R	1.0	0.041 ± 0.015	2.8	0.081 ± 0.017	4.8	1.8
Local U-R	1.1	0.026 ± 0.015	1.7	0.080 ± 0.017	4.8	2.4

[a] Mass in $\log(M_{\rm stellar}/M_{\odot})$
[b] Significance is quadrature sum.
[c] Difference is the quadrature sum difference in Hubble residual step magnitudes between red and blue subsamples.

Table A3. Subsample r.m.s when splitting the sample based on c using a 5D bias correction.

Property		$c<0$ Hubble Residual r.m.s.		$c>0$ Hubble Residual r.m.s.	
Name	Division Point	$<DP$[b]	$>DP$	$<DP$	$>DP$
Global Mass[a]	10.0	0.138 ± 0.019	0.160 ± 0.016	0.199 ± 0.025	0.179 ± 0.016
Local Mass	9.4	0.133 ± 0.015	0.174 ± 0.021	0.184 ± 0.019	0.189 ± 0.020
Global U-R	1.0	0.135 ± 0.016	0.165 ± 0.018	0.193 ± 0.021	0.180 ± 0.018
Local U-R	1.1	0.133 ± 0.016	0.168 ± 0.019	0.195 ± 0.020	0.177 ± 0.019

[a] Mass in $\log(M_{\rm stellar}/M_{\odot})$
[b] DP refers to the 'Division Point' location of the environmental property step. For example, '<DP' indicates the lower mass or bluer environments.

APPENDIX A: BBC5D

In this analysis, we have focused on using a BBC1D bias correction, however for completeness and consistency with K21, here we discuss the differences in results when using a BBC5D bias correction. When using BBC5D, three fewer SNe Ia pass our quality cuts, resulting in a sample of 672. Using SALT2 (Section 2.1.1), we obtain values of $\alpha = 0.164 \pm 0.009$ and $\beta = 3.36 \pm 0.07$ for this sample.

For the overall environmental property steps, as presented in Table A1, there is little difference in magnitude or significance, with only a slight decrease (~ 0.01 mag) for BBC5D. The Hubble residual r.m.s. values decrease for all properties and for each side of the division point, but more so on the right hand side (higher $M_{\rm stellar}$ or redder). This results in smaller differences in the r.m.s. values either side of the steps for BBC5D than for BBC1D, indicating that the additional corrections of BBC5D are absorbing some of the dispersion.

As presented in Table A2, when splitting the data based on c, we find that our three lost SNe all had $c > 0$. Interestingly, the step sizes remain fairly consistent for the $c < 0$ SNe Ia, but BBC5D exhibits noticeably smaller step sizes for $c > 0$ than BBC1D. This results in slightly less significant differences between red and blue SNe using BBC5D.

As above, the r.m.s. values across the board decreased using BBC5D (indicative of the increased scatter when only applying a redshift correction as in BBC1D), shown in Table A3. As with the step sizes, the r.m.s. values for $c > 0$ decrease more, resulting in an smaller difference between the r.m.s. values between red and blue SNe using BBC5D. This is particularly noticeable when comparing the blue SNe in low $M_{\rm stellar}$ or blue environments with those that are not, and is clear to see in Figure A1.

As in Section 4.2, we fit for trends between the observed environmental property c dependent Hubble residual relationships. The resulting trends for global $M_{\rm stellar}$ and $U-R$ are presented in Figure A2. As can be seen, the relationships are not identical to those using BBC1D, but they do follow the same general trends.

Presented in Table A4 are the remaining environmental property Hubble residual steps when these c-dependent trends have been corrected for using the BBC5D bias correction. These remaining step values are fairly consistent with BBC1D, suggesting that our findings are not a result of the bias correction used. This agrees with Section 3, that a c-dependent global $U-R$ correction achieves the greatest reduction of remaining Hubble residual dispersion. Correcting for a c - global $M_{\rm stellar}$ still results in an intriguing 2σ remaining $U-R$ step.

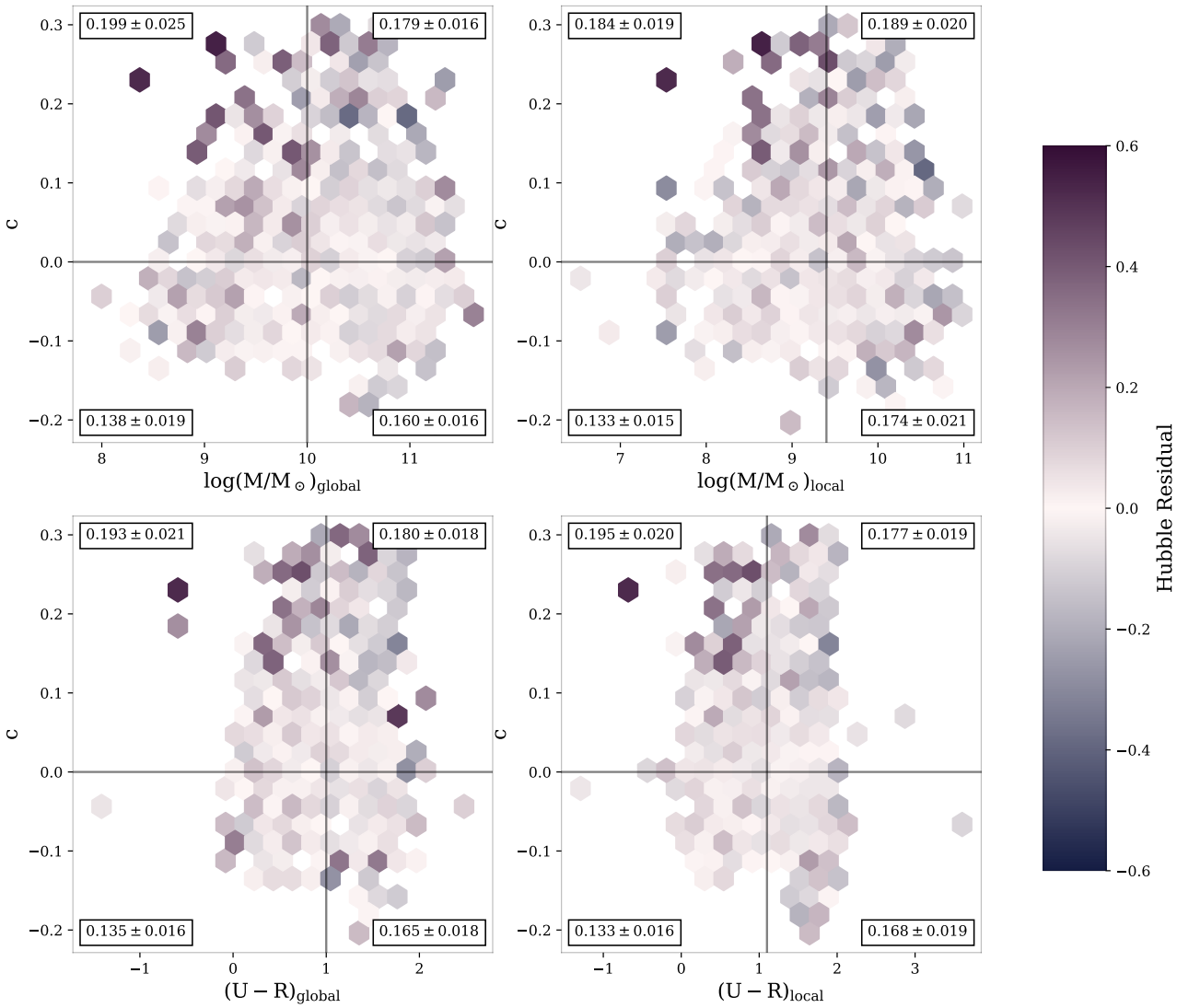

Figure A1. As Figure 5, but using a BBC5D bias correction.

Table A4. Magnitudes and significances of remaining environmental property steps when fitting for relationships between c and environmental properties, using a 5D bias correction.

		Fitting For:			
		Host Mass	Local Mass	Host U-R	Local U-R
Remaining Step In:	Host Mass	0.002±0.012 0.1σ	0.036 ± 0.012 3.0σ	0.013±0.012 1.1σ	0.021±0.012 1.7σ
	Local Mass	0.007 ± 0.011 0.6σ	0.000 ± 0.011 0.0σ	0.005 ± 0.011 0.4σ	0.004 ± 0.011 0.4σ
	Host U-R	0.023±0.011 2.0σ	0.041 ± 0.011 3.7σ	0.001±0.011 0.1σ	0.017±0.011 1.5σ
	Local U-R	0.018±0.011 1.6σ	0.032 ± 0.011 2.8σ	0.005±0.011 0.4σ	0.001±0.011 0.1σ

All steps given in mag.
Step division points as described in Section 4.1.

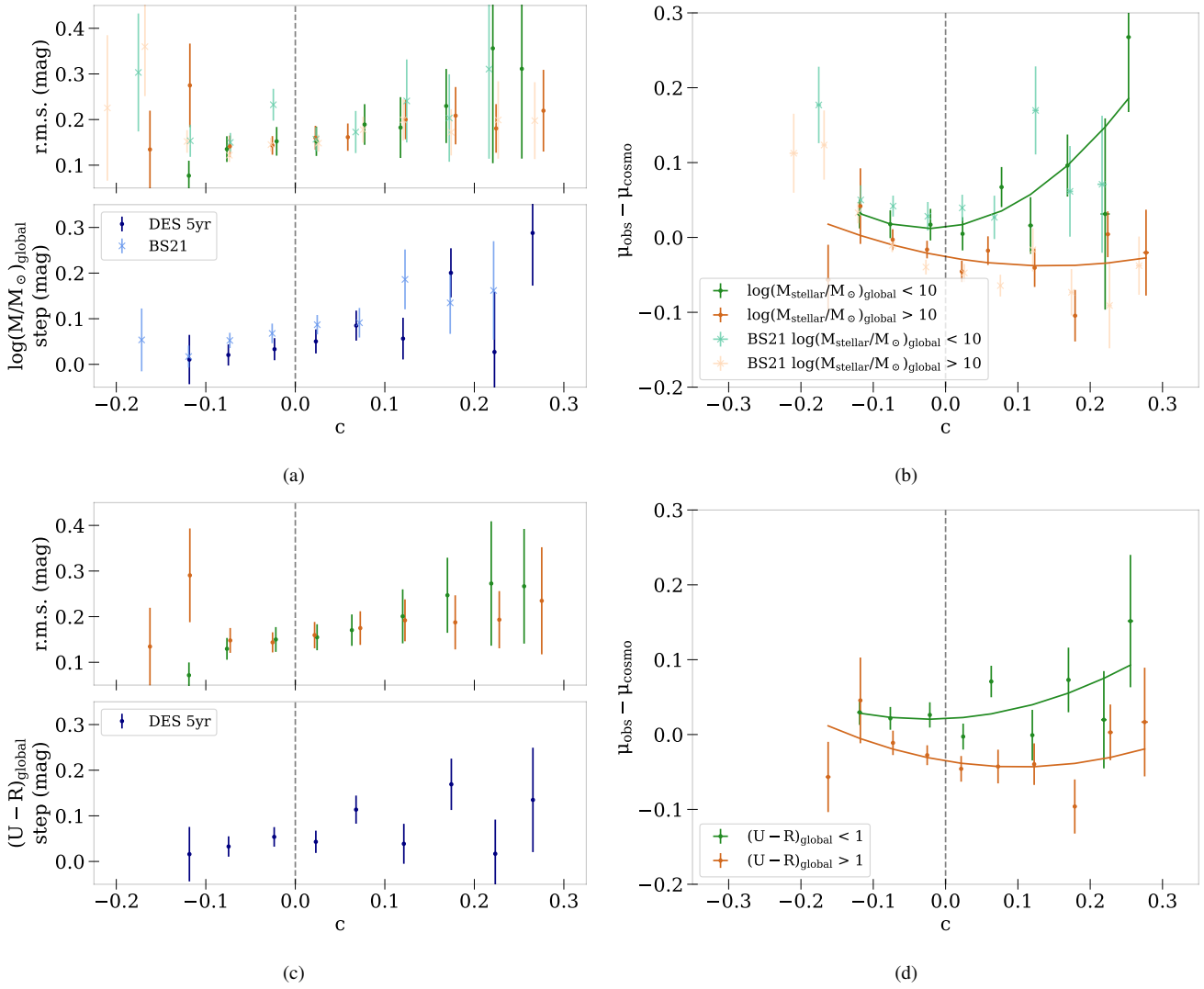

Figure A2. As Figure 6, but using a BBC5D bias correction.

APPENDIX B: DIFFERENT CLASSIFIERS AND TRAINING SETS

For this analysis, we have focused on using the SuperNNova (SNN) (Möller & de Boissière 2020) photometric classifier trained on core-collapse templates from Vincenzi et al. (2019), requiring $P(Ia) > 0.5$ as this is currently the preferred choice for the final DES5YR sample within the DES-SN collaboration. However, we repeated this analysis using various combinations of classifier, templates and probability cuts. These are defined as follows:

(i) SNN trained on Vincenzi et al. (2019) templates, $P(Ia) > 0.5$
(ii) SNN trained on Vincenzi et al. (2019) templates, $P(Ia) > 0.8$
(iii) SNN trained on Vincenzi et al. (2019) templates, $P(Ia) > 0.95$
(iv) SNN trained on Jones et al. (2017) templates, $P(Ia) > 0.5$
(v) SNN trained on Hounsell & Sako (2022) templates, $P(Ia) > 0.5$
(vi) Supernova Identification with Random Forest (SNIRF; an extension of Dai et al. 2018) trained on Vincenzi et al. (2019) templates, $P(Ia) > 0.5$
(vii) SNIRF trained on Jones et al. (2017) templates, $P(Ia) > 0.5$

The overwhelming majority of candidate objects have a high probability of being a SNe Ia of $P(Ia) > 0.95$. When the different $P(Ia)$ samples undergo the additional quality cuts that are specific to this analysis, the final sample sizes were comparable, and there was no real difference in results for each sample. In other words, the objects that had a low $P(Ia)$ typically also had the largest uncertainties in x_1, c, and environmental properties, meaning that they were removed in each case.

This paper has been typeset from a TEX/LATEX file prepared by the author.